The Astrophysical Journal, 836:241 (18pp), 2017 February 20 https://doi.org/10.3847/1538-4357/aa5c80

High-energy Emissions from the Pulsar/Be Binary System PSR J2032+4127/MT91 213

J. Takata[1], P. H. T. Tam[2], C. W. Ng[3], K. L. Li[4], A. K. H. Kong[5], C. Y. Hui[6], and K. S. Cheng[3]
[1] School of physics, Huazhong University of Science and Technology, Wuhan 430074, China; takata@hust.edu.cn
[2] Institute of Astronomy and Space Science, Sun Yat-Sen University, Guangzhou 510275, China
[3] Department of Physics, The University of Hong Kong, Pokfulam Road, Hong Kong
[4] Department of Physics and Astronomy, Michigan State University, East Lansing, MI 48824-2320, USA
[5] Institute of Astronomy and Department of Physics, National Tsing Hua University, Hsinchu, Taiwan
[6] Department of Astronomy and Space Science, Chungnam National University, Daejeon 305-764, Korea
Received 2016 October 1; revised 2017 January 13; accepted 2017 January 23; published 2017 February 24

Abstract

PSR J2032+4127 is a radio-loud gamma-ray-emitting pulsar; it is orbiting around a high-mass Be type star with a very long orbital period of 25–50 years, and is approaching periastron, which will occur in late 2017/early 2018. This system comprises a young pulsar and a Be type star, which is similar to the so-called gamma-ray binary PSR B1259–63/LS2883. It is expected therefore that PSR J2032+4127 shows an enhancement of high-energy emission caused by the interaction between the pulsar wind and Be wind/disk around periastron. Ho et al. recently reported a rapid increase in the X-ray flux from this system. In this paper, we also confirm a rapid increase in the X-ray flux along the orbit, while the GeV flux shows no significant change. We discuss the high-energy emissions from the shock caused by the pulsar wind and stellar wind interaction and examine the properties of the pulsar wind in this binary system. We argue that the rate of increase of the X-ray flux observed by *Swift* indicates (1) a variation of the momentum ratio of the two-wind interaction region along the orbit, or (2) an evolution of the magnetization parameter of the pulsar wind with the radial distance from the pulsar. We also discuss the pulsar wind/Be disk interaction at the periastron passage, and propose the possibility of formation of an accretion disk around the pulsar. We model high-energy emissions through the inverse-Compton scattering process of the cold-relativistic pulsar wind off soft photons from the accretion disk.

Key words: methods: numerical – methods: observational – pulsars: individual (PSR J2032+4127) – radiation mechanisms: non-thermal – stars: massive – X-rays: binaries

1. Introduction

PSR J2032+4127 is a radio-loud gamma-ray-emitting pulsar discovered by the *Fermi* Large Area Telescope (*Fermi*-LAT) and is a young pulsar with a spin period $P = 143$ ms, spin-down power $L_{\rm sd} \sim 1.7 \times 10^{35}$ erg s^{-1} and spin-down age $\tau \sim 180$ kyr (Abdo et al. 2013). This pulsar had been regarded as isolated (Camilo et al. 2009) because of the lack of apparent variation in its rotation caused by reasonable orbital motion. Lyne et al. (2015) found the variation of the observed pulsar rotation rate, which is consistent with the Doppler effect of the orbital motion around the high-mass Be star MT91 213. Their study suggests that the orbital period is very long, $P_{\rm ob} \sim 25$ yr, and the orbit is extremely elongated with an eccentricity $e \sim 0.93$. Ho et al. (2017) refined the orbit parameters as $P_{\rm ob} \sim 50$ years and $e \sim 0.96$ (see Figure 1). PSR J2032+4127 is a member of a class of rare-type pulsars orbiting a high-mass B star. The next periastron passage will occur in late 2017 or early 2018.

The binary nature of PSR J2032+4127 is similar to that of PSR B1259–63, which is a well known radio pulsar orbiting around the high-mass B star, LS2883, with $P_{\rm ob} \sim 3.4$ years and $e \sim 0.83$ (Johnston et al. 1992, 1999, 2005). PSR B1259–63/LS2883 is known to be a source of non-pulsed and non-thermal emissions in the X-ray/GeV/TeV bands (Aharonian et al. 2005; Abdo et al. 2011; Tam et al. 2011, 2015), and it is classified as a so-called gamma-ray binary, which comprises a compact object (neutron star or black hole) and a high-mass OB star (see Dubus 2013). Multi-wavelength observations have confirmed several TeV gamma-ray binaries, namely, PSR B1259–63/LS 2883, LS5039 (Aharonian et al. 2006), LS I+61° 303 (Albert et al. 2006), 1FGL J1018.6-5856 (Ackermann et al. 2012), and H.E.S.S. J0632+057 (Hinton et al. 2009). PSR B1259–63/LS 2883 is the only binary system for which the compact object has been confirmed to be a young pulsar. PSR J2032+4127/MT91 213 is a candidate for the next gamma-ray binary, for which the compact object is definitely a young pulsar.

The origin of the high-energy TeV emissions from the PSR B1259–63/LS 2883 system is likely related to the interaction of the pulsar wind of PSR B1259–63 and the Be wind/disk of LS 2883 (Tavani & Arons 1997; Dubus 2006, 2013). Their interaction results in the formation of a shock, where the ram pressures of the pulsar wind and of the stellar wind/disk are in balance (Figure 2). The electrons/positrons in the pulsar wind are accelerated at the shock, and produce non-thermal emission in the radio to TeV gamma-ray bands. The standard scenario assumes synchrotron radiation and the inverse-Compton scattering (ICS) process produces radio/X-ray emission and TeV gamma-ray emission. We can expect that PSR J2032+4127/MT91 213 is also a source of X-rays/TeV gamma-rays arising from the same mechanisms.

X-ray/TeV emissions from gamma-ray binaries have been observed to exhibit temporal variations in their emission. Various models have been suggested to explain the energy-dependent orbital modulations: for the pulsar model of gamma-ray binaries, for example, the Doppler boosting effect due to the finite velocity of the shocked pulsar wind (Dubus et al. 2010; Kong et al. 2012; Takata et al. 2014a), evolution of the energy spectra of relativistic electrons of the shocked pulsar wind under different energy-loss rates (Khangulyan et al. 2007; Takahashi et al. 2009; Zabalza et al. 2013), and the interaction between the pulsar wind and the Be disk (Sierpowska-Bartosik

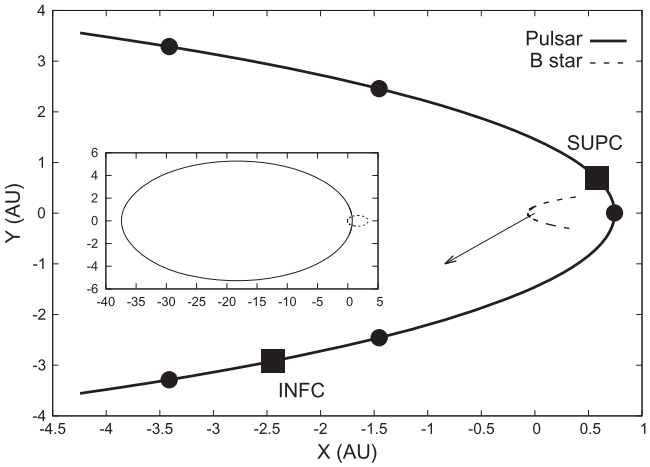

Figure 1. Schematic diagram illustrating the orbit of PSR J2032+4127 (solid line) and B star companion MT91 21 (dashed line) around the periastron, viewed from perpendicular to the orbit plane. The orbit parameters are $P_{\rm ob} = 17{,}000$ days and $e = 0.961$ (Ho et al. 2017). The main panel and inserted panel show the orbit during −250 and 250 days from the periastron and entire orbit, respectively. The filled circles mark 100 day intervals. The arrows indicate the direction to the Earth, and the boxes show the positions of the inferior conjunction (INFC) and superior conjunction (SUPC), respectively.

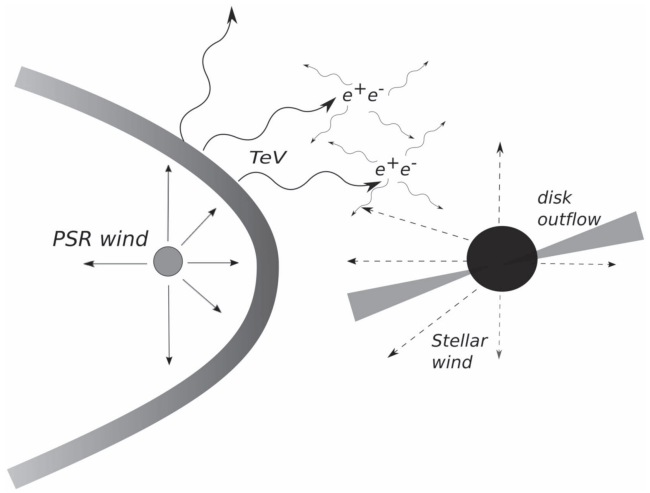

Figure 2. Schematic picture of the interaction of the pulsar wind and Be wind/disk. The synchrotron process and ICS process of the shocked pulsar wind produce X-rays and TeV gamma-rays, respectively. The TeV gamma-rays may create new electron and positron pairs by the photon–photon pair-creation process, and they initiate a pair-creation cascade if they propagate toward the companion star.

& Bednarek 2008; Takata et al. 2012) have been suggested. In this paper, we will consider the orbital variation of the emission from PSR J2032+4127/MT91 213 as a result of the radial evolution of the magnetization parameter (Takata & Taam 2009; Kong et al. 2011) or the variation of the momentum ratio of the two winds.

The GeV emission from PSR J2032+4127/MT91 213 is modulating with the spin period of the pulsar, and hence is dominated by the magnetospheric process. The GeV emission from gamma-ray binaries has been observed by *Fermi*-LAT. For PSR B1259–63/LS 2883, flare-like GeV emissions have been observed after the second Be disk passage of the pulsar (Abdo et al. 2011; Tam et al. 2011, 2015). Although the ICS process with anisotropic soft-photon field from the disk/companion star (e.g Khangulyan et al. 2011, 2014; van Soelen et al. 2012; Dubus & Cerutti 2013) or synchrotron radiation process of the relativistic electrons/positrons (Chernyakova et al. 2015; Xing et al. 2016) have been considered, the origin of the emission is not yet understood.

The gamma-binary LS 5039, whose orbital period is 3.9 days, is a candidate for which the compact object is a young pulsar. The GeV emission from this system has been observed over the whole orbital phase by *Fermi*-LAT (Abdo et al. 2009). Because the spectral shape measured by *Fermi* resembles those of the gamma-ray emitting pulsars, it has been suggested that LS 5039 includes a young pulsar. The orbital modulating GeV emission confirmed by *Fermi*, however, suggests the emission process being in the intra-binary space. The orbital modulations of GeV and X-ray/TeV emissions from LS 5039 show anti-correlation: the GeV flux (or X/TeV fluxes) becomes maximum around the superior conjunction (hereafter SUPC) (or inferior conjunction (INFC)) and becomes minimum around the INFC (or SUPC). Within the framework of the shock emission due to the interaction between the pulsar and stellar winds, the observed modulation of the X-ray emission from LS 5039 has been interpreted as a Doppler boosting effect caused by the finite velocity of the shocked pulsar wind (Dubus et al. 2010; Takata et al. 2014a), while the strong absorption of the TeV photons by the stellar photon field will suppress the observed emission around the SUPC (Dubus et al. 2008). The GeV emission may be a result of the ICS process of the cold-relativistic pulsar wind (Sierpowska-Bartosik & Torres 2008; Kapala et al. 2010; Torres 2011; Takata et al. 2014a) or of the shock-accelerated particles (Yamaguchi & Takahara; Zabalza et al. 2013). The ICS process between the relativistic particles and the stellar photons causes a flux peak in the observed modulation around the SUPC (if there is no absorption), where the scattering process of the relativistic particles that propagate to the Earth occurs head-on, and causes a flux minimum around the INFC, where the scattering is a tail-on collision process. In this paper, we will estimate the contribution of the ICS process to the cold-relativistic pulsar wind and stellar photons, since the gamma-ray binary will provide a unique laboratory to investigate the properties of the cold-relativistic pulsar wind at the au distance scale from the pulsar (Cerutti et al. 2008).

The bolometric luminosity of the high-mass companion in gamma-ray binaries is of the order $L_* \sim 10^{38}$ erg s^{-1}. This intense stellar photon field leads to not only observable TeV emissions through the ICS, but also substantial $\gamma\gamma$ absorption of TeV gamma-rays. Because the stellar radiation field is anisotropic in the emission region, the emissivity of the ICS and optical depth of the photon–photon pair-creation process integrated along the line of sight depend on the orbital phase. Such anisotropic processes will cause the observed orbital modulation of TeV gamma-rays (e.g., Kirk et al. 1999; Bednarek 2000; Takata et al. 2014a). The secondary pairs created by the primary TeV gamma-rays are also a source of very high-energy photons through the ICS process. A pair-creation cascade process may develop in the stellar wind region and may cause the observed TeV emissions from close binary systems (Bednarek 1997, 2007; Sierpowska & Bednarek 2005; Sierpowska-Bartosik & Torres 2007, 2008) and the periastron passage of long-orbit binaries (Sierpowska-Bartosik & Bednarek 2008). The anti-correlation between the GeV and

TeV light curves of LS 5039 has been interpreted using this cascade model (Bednarek 2007).

In the X-ray bands, the observed temporal variations along the orbit will be mainly caused by the variations of the physical conditions of the pulsar wind at the shock. With the extremely elongated orbit of PSR B1259–63 and PSR J2032+4127, the distance of the shock (r_s) from the pulsar varies by about a factor of ten along the orbit (Figure 5). Hence we can in principle use gamma-ray binaries to probe the physical properties of the pulsar wind (e.g., magnetization parameter and bulk Lorentz factor) as a function of radial distance. For example, the pulsar wind magnetization parameter (Kennel & Coroniti 1984) can be determined as

$$\sigma(r_s) = \frac{B_1^2}{4\pi\Gamma_{\rm PW,0} N_1 m_e c^2}, \quad (1)$$

where, B_1, N_1 and $\Gamma_{\rm PW,0}$ are the magnetic field, number density and Lorentz factor of the cold-relativistic pulsar wind, respectively, just before the shock. We can probe how the magnetization parameter changes with the radial distance from the pulsar by examining the observed temporal variations (Takata & Taam 2009; Kong et al. 2011). Since PSR J2032 +4127 is now approaching the periastron passage that will occur in late 2017 or early 2018, and since the separation between PSR J2032+4127 and MT91 213 changes by about a factor of ten over ~ -1 year and $\sim +1$ year from the periastron (Figures 1 and 5), we can expect that the change of the shock distance from the pulsar will cause a large variation in the observed emission from this system, as indicated by the results of the recent X-ray observations of *Swift* (Section 2, see also Ho et al. 2017). Moreover, the ICS process of the cold-relativistic pulsar wind before the shock may boost the stellar photons from optical to gamma-ray bands. The next periastron passage may provide us with a unique opportunity to constrain the Lorentz factor $\Gamma_{\rm PW,0}$ of the pulsar wind.

This paper is organized as follows. In Section 2, we will analyze the data taken from *Swift* and *Fermi*-LAT. We will confirm that the X-ray emission observed in 2016 is about factor of ten larger than that from previous observations, while the GeV flux does not show any significant change. In Section 3, we describe our emission models from the intra-binary shock and cold-relativistic pulsar wind. In Section 4, we will discuss the high-energy emission within the framework of the pulsar wind/Be wind, and probe the evolution of the magnetization parameter with radial distance by fitting the *Swift* data. In Section 5, we will discuss the emission as a result of the pulsar wind/Be disk interaction model. We will also discuss the possibility of the formation of an accretion disk around the pulsar as a consequence of the pulsar/Be disk interaction and its expected emission in the high-energy bands.

2. Data Analysis of *Swift* and *Fermi* Observations

Recently, Ho et al. (2017) reported a rapid increase in the X-ray flux observed by *Swift*, as the pulsar approached periastron. In this paper, we analyze the *Fermi*-LAT as well as the *Swift*data. The *Swift* X-ray telescope (XRT) light curve was obtained using products extracted from the XRT repository http://www.swift.ac.uk/user_objects/ (see also Evans et al. 2007, 2009). We used a conversion factor of 1.27×10^{-10} erg cm^{-2} ct^{-1} to convert the count rates into unabsorbed fluxes, where an absorbed power-law with $\Gamma_X = 2.37$ and $n_{\rm H} = 1.4 \times 10^{22}$ cm^{-2}, based on total galactic HI column density in the direction toward the pulsar, is assumed (Dickey & Lockman 1990; Kalberla et al. 2005). Since Ho et al. (2017) adopted $n_{\rm H} = 7.7 \times 10^{21}$ cm^{-2} based on the optical extinction of the companion, our unabsorbed X-ray flux is slightly higher than that presented by those authors. This difference does not affect the conclusions of the model calculations discussed in this paper. Due to the small photon statistics, we did not include observations shorter than 10 ks before 2014. An observation taken in 2006 had an instrumental issue and was also not included. An X-ray light curve is shown in Figure 3. Following up on the initial flux increase observed in early 2016, we asked for additional dedicated XRT ToO observations from 2016 March. Three to four observations were grouped together for better signal-to-noise ratios. It is clear that the trend in 2016 is the X-ray flux increase.

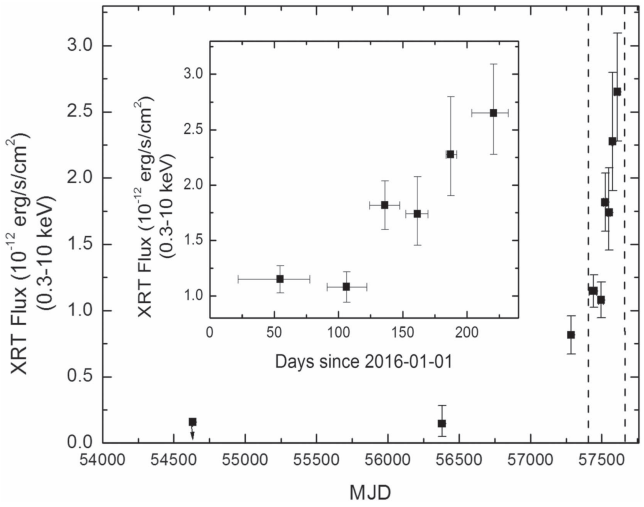

Figure 3. Main figure: the long-term *Swift*/XRT flux evolution. Inset: the flux evolution in 2016, showing an increase in X-ray flux. Details on how to obtain the data are described in Section 2.

We analyzed the gamma-ray long-term light curve of PSR J2032+4127 using data from *Fermi*-LAT. Photon events with energy ranging from 100 MeV to 500 GeV and time ranging from 2008 August 4 to 2016 August 2 were selected. The event class is "Pass 8 Source" and the corresponding instrumental response function is "P8R2_SOURCE_V6." The region of interest (ROI) is a 20° × 20° square centered at the epoch J2000 position of the source: (R.A., decl.) = ($20^{\rm h}32^{\rm m}14\overset{\rm s}{.}35$, $+41°26'48\overset{''}{.}8$). To avoid contamination from the Earth's albedo, we excluded the time intervals when the ROI was observed at a zenith angle greater than 90°. The data reduction in this study was performed using the *Fermi* Science Tools package version v10r0p5.[7]

We first modeled the average emission from the background sources over the whole time span. The *gtlike* tool was used to perform a maximum binned likelihood analysis. The source model includes all 3FGL catalog sources (gll_psc_v16.fit) (Acero et al. 2015) that are within 25° from the center of the ROI, the galactic diffuse emission (gll_iem_v06) and the isotropic diffuse emission (iso_P8R2_SOURCE_V6_v06),

[7] Available at http://fermi.gsfc.nasa.gov/ssc/data/analysis/software/.

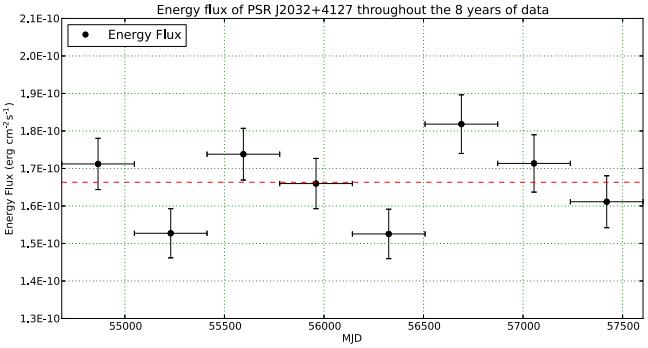

Figure 4. The long-term *Fermi* flux evolution. The horizontal line shows the average flux over the eight-year observations, $F_\gamma = 1.65 \pm 0.07 \times 10^{-10}$ erg cm^{-2} s^{-1}.

available from the *Fermi* Science Support Center (FSSC).[8] The spectral parameters for sources that are non-variable and located 5° away from the center are fixed to their catalog values. Four extended sources within the region, Gamma Cygni, Cygnus Cocoon, HB 21, and Cygnus Loop, were modeled by the extended source templates provided by the FSSC. PSR J2032+4127 is named as 3FGL J2032.2+4126 in the 3FGL catalog and is modeled by a power-law with simple exponential cutoff:

$$\frac{dN}{dE} = N_0 \left(\frac{E}{E_0}\right)^{-\Gamma} \exp\left(-\frac{E}{E_C}\right), \quad (2)$$

where N_0 is the normalization constant, E_0 is the scale factor of energy, Γ is the spectral power-law index and E_C is the cut-off energy. From the binned likelihood analysis, the best-fit parameters of PSR J2032+4127 are $N_0 = (1.70 \pm 0.05) \times 10^{-11}$ ph erg^{-1} cm^{-2} s^{-1}, $\Gamma = -1.43 \pm 0.03$ and $E_C = 4500 \pm 259$ MeV.

After fixing the spectral indices of all sources to the global fit and only leaving the normalization parameters free, the source model is then used to obtain the long-term light curve. The whole data set is then binned into eight bins, each of 365 days. The energy range of the photons is further limited to 100 MeV–100 GeV. Local fit is performed by the *gtlike* tool (binned likelihood analysis) to obtain the energy flux of PSR J2032+4127 in each segment. Figure 4 shows the long-term evolution of the flux measured by *Fermi*. No clear indication of the change in the flux can be seen and the average flux over the eight-year observations is $F_\gamma = 1.65 \pm 0.07 \times 10^{-10}$ erg cm^{-2} s^{-1}, which will be dominated by pulsed emissions from the magnetosphere.

In the 1990s, CGRO/EGRET observed the region of PSR J2032+4127 a couple of times, including a more intensive observation during 1994 May to July. There is one source in the revised EGRET catalog (Casandjian & Grenier 2008), EGR J2033+4117, whose position is 0.28 deg away from 3FGL J2032.2+4126 (which has been identified as PSR J2032+4127). The 95% error radius of EGR J2033+4117 is 0.22 deg. Due to the slight offset, we cannot associate the two gamma-ray sources for certain.

It is still possible to constrain the gamma-ray emission from PSR J2032+4127 using these EGRET data. The photon flux of EGR J2033+4117 is steady over several measurements, and is consistent with (5–6) $\times 10^{-7}$ph cm^{-2} s^{-1} (above 100 MeV) for all viewing periods. Due to the poorer angular resolution of EGRET compared to LAT, and allowing for plausible contamination from nearby sources like Cyg X-3, this flux level may be regarded as an upper limit of any source at the position of PSR J2032+4127 during the 1990s, and is above the average LAT flux $\sim 1.4 \times 10^{-7}$ ph cm^{-2} s^{-1} in our analysis.

[8] http://fermi.gsfc.nasa.gov/ssc/

3. Theoretical Model

The origin of the high-energy TeV emission from the PSR B1259–63/LS 2883 system is likely related to the interaction of the pulsar wind of PSR B1259–63 and the Be wind/disk of LS 2883 (Tavani & Arons 1997). Their interaction results in the formation of a shock, where the pulsar wind ram pressure and stellar wind/disk ram pressure are in balance. We apply this scenario to the PSR J2032+4129/MT91 213 binary. In this section we describe our calculation methods. We define the capital letter R and small letter r as the distances from the B star and from the pulsar, respectively.

3.1. Pulsar Wind/Stellar Wind Interaction

The relativistic pulsar wind, which may have a bulk Lorentz factor of $\Gamma_{\rm PW,0} \sim 10^{3-6}$, interacts with the stellar wind and forms a cone-shaped shock separating the pulsar and the companion star. The radial distance to and its opening angle of the cone-shaped shock are determined by the ratio of the two winds (e.g., Canto et al. 1996 and reference therein),

$$\eta \equiv \frac{L_{\rm sd}}{\dot{M}_w v_w c}, \quad (3)$$

where we assume that the pulsar wind carries the spin-down power $L_{\rm sd}$ of the pulsar, $\dot{M}_w$ and v_w is the mass loss rate and wind velocity of the companion star, respectively. The wind velocity of the stellar wind at a distance R from the stellar surface may be expressed by (Waters et al. 1988)

$$v_w(R) = v_0 + (v_\infty - v_0)(1 - R_*/R). \quad (4)$$

where $v_0 \sim \sqrt{3kT_s/m_p} \sim 28$ km with $T_s \sim 30{,}000$ K being the temperature of the B star. The terminal velocity is estimated from

$$v_\infty \sim \sqrt{\frac{2GM_*}{R_*}} \sim 8 \times 10^7 \,{\rm cm\,s^{-1}} \left(\frac{M_*}{15M_\odot}\right)^{1/2} \left(\frac{R_*}{10R_\odot}\right)^{-1/2}$$

with M_* and R_* being the mass and radius of the B star, respectively. Since the shock is far away from the surface of the B star, we may assume $v_w(R_s) = v_\infty$.

With $L_{\rm sd} = 1.7 \times 10^{35}$ erg s^{-1} of this pulsar (Lyne et al. 2015) and a typical mass loss rate $\dot{M}_w \sim 10^{-9}$–$10^{-7} M_\odot$ yr^{-1} of an O-type or B-type star (e.g., Snow 1981; Smith 2006), the momentum ratio of this system will be

$$\eta \sim 0.085 \left(\frac{L_{\rm sd}}{1.7 \cdot 10^{35}\,{\rm erg\,s^{-1}}}\right)\left(\frac{\dot{M}_w}{10^{-8}M_\odot\,{\rm yr^{-1}}}\right)^{-1} \times \left(\frac{v_w}{10^{-8}\,{\rm cm\,s^{-1}}}\right)^{-1}, \quad (5)$$

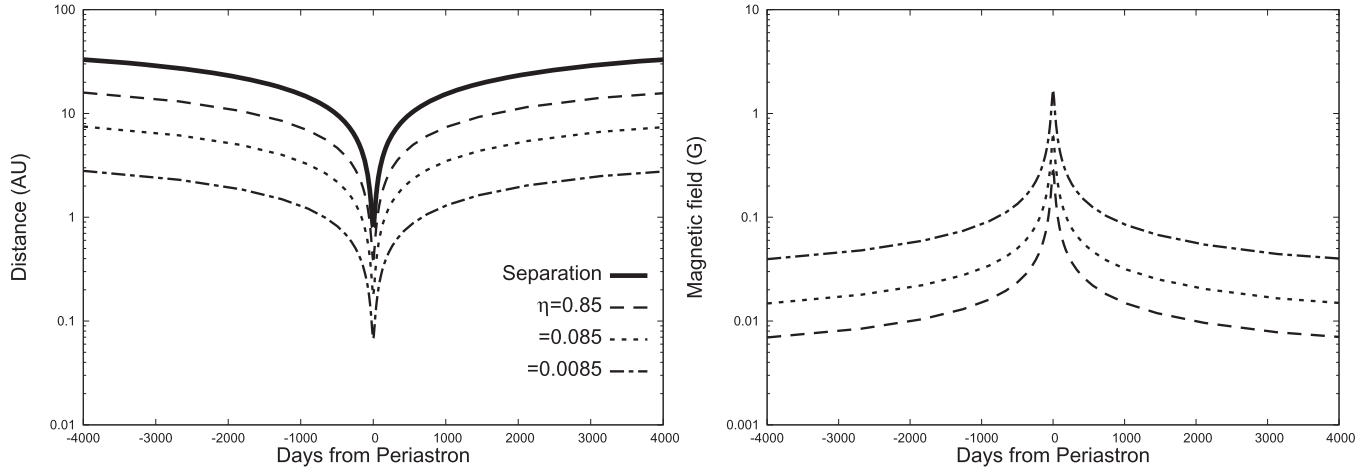

Figure 5. Left: separation between the pulsar and B star (solid line), and the shock distance from the pulsars along the orbit between −4000 days and +4000 days from periastron. The dashed ($\eta = 0.85$), the dotted ($\eta = 0.085$) and the dashed–dotted ($\eta = 0.0085$) correspond to the cases for $\dot{M}_w = 10^{-9} M_\odot$ yr^{-1}, $10^{-8} M_\odot$ yr^{-1} and $10^{-7} M_\odot$ yr^{-1}, respectively, with Equation (5) and $v_w = 10^8$ cm s^{-1}. Right: the magnetic field strength at periastron at the shock apex for $\eta = 0.85$ (dashed line), 0.085 (dotted line) and 0.0085 (dashed dotted line), respectively. The magnetization parameter at the shock is assumed to be $\sigma(r_s) = 0.1$.

indicating that the stellar wind is stronger than the pulsar wind with a reasonable mass loss rate of the former. The distance to the apex of the shock cone, r_s, and the opening angle of the shock, θ_s, measured by the pulsar are calculated from (Canto et al. 1996)

$$r_s(\phi) = \frac{\eta^{1/2}}{1 + \eta^{1/2}} a(\phi) \tag{6}$$

and

$$\theta_s(\eta) - \tan\theta_s(\eta) = \frac{\pi}{1 - \eta}, \tag{7}$$

respectively, where ϕ represents the orbital phase and $a(\phi)$ is the separation between the two stars. Figure 5 summarizes the evolution of the distance (left panel) and the magnetic field strength (right panel) at the shock apex along the orbit between −4000 days and +4000 days from periastron (we did not plot the results for the other orbital phase, since we are interested in the emission processes around periastron). In the figure, we used $\sigma(r_s) = 0.1$ to calculate the magnetic field strength. As the figure shows, the shock distance and the magnetic field at the shock change by more than factor of ten along the orbit. Since the pulsar orbit velocity ($v_p \sim 10^{6-7}$ cm s^{-1}) is at least about a factor of ten slower than the stellar wind velocity ($v_w \sim 10^8$ cm s^{-1}), we assume that the shape of the shock cone is axially symmetric about the axis connecting the two stars.

3.2. Pulsar/Be Disk Interaction

Since the Be-type star, MT91 213, forms a dense equatorial disk outflow, the pulsar may interact with the Be disk at the periastron passage, as in the case with the gamma-ray binary PSR B1259–63/LS2883 system. The decretion disk model has been explored to describe the structure of the Be disk (Lee et al. 1991; Carciofi & Bjorkman 2006; Okazaki et al. 2011), and it implies a disk mass density (ρ_d) and a scale height (H) described by

$$\rho_d(R, z) = \rho_0 \left(\frac{R_*}{R}\right)^n \exp\left(-\frac{z^2}{2H^2}\right), \tag{8}$$

and

$$H(R) = H_0 \left(\frac{R}{R_*}\right)^\beta, \tag{9}$$

respectively, where $n \sim 3$–3.5 and $\beta \sim 1$–1.5 ($n = 3.5$ and $\beta = 1.5$ for an isothermal disk). In addition, we apply $H_0 \sim 0.02 R_*$ and the base density $\rho_0 \sim 10^{-11}$–10^{-9} g cm^{-3}.

Takata et al. (2012) studied the orbital modulations of the X-ray/TeV emission from the PSR B1259–63/LS2883 system. They argued that with the larger base density ($\rho_0 \sim 10^{-9}$ g cm^{-3}) for the Be disk, the pulsar wind creates a cavity in the disk gas and this causes a significant increase in the conversion efficiency from pulsar spin-down power to the shock-accelerated particle energy. This explains the double-peak structure of the X-ray light curves of PSR B1258-63/LS 2883. The pulsar/Be disk interaction with a smaller base density ($\rho_0 < 10^{-10}$ g cm^{-3}) causes no cavity in the pulsar wind and hence no enhancement in the emission.

With the elongated orbit and the long orbital period of PSR J2032+4127, a strong pulsar/Be disk interaction will be possible only at periastron passage. The radius of the shock from the pulsar may be obtained from the pressure balance condition,

$$r_s = \left(\frac{L_{\rm sd}}{2\pi \rho_d v_r^2 c}\right)^{1/2}, \tag{10}$$

where v_r is the relative velocity between the pulsar and the disk rotation. If the pulsar interacts with the Be disk at periastron, where the separation of the two stars is $a \sim 1$ au, the mass density and scale height of the disk at the pulsar are $\rho(a) \sim 2 \times 10^{-5} \rho_0$ and $H(a) \sim 10^{12}$ cm, where we used $n = 3.5$, $\beta = 1.5$, $H_0 = 0.02 R_*$ and $R_* = 10 R_\odot$. The orbital velocity of the pulsar and circular velocity of the disk are $v_p \sim 10^7$ cm s^{-1} and $v_{d,K}(a) = v_{d,K}(R_*)(R_*/1\ {\rm au})^{1/2} \sim 10^7$ cm s^{-1}, respectively, where we

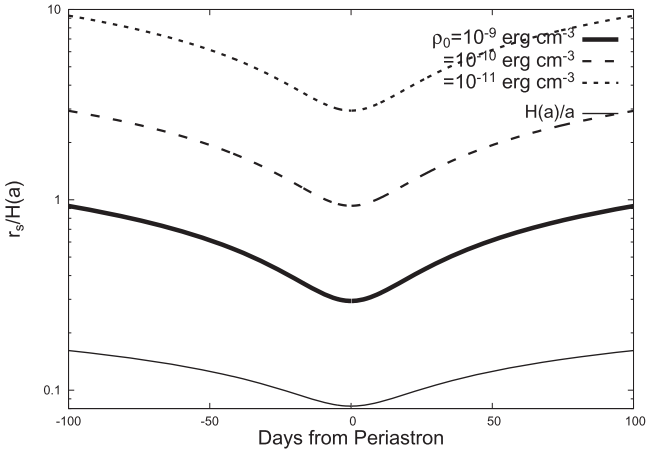

Figure 6. Shock distance (Equation (10)) for the pulsar/Be disk interaction, if the pulsar interacts with the Be disk at the given orbit phase (x-axis). The disk structure is calculated using $n = 3.5$, $\beta = 1.5$, $H_0 = 0.02R_*$ and circular velocity $v_{d,K} = 500\ \mathrm{km\ s^{-1}}(R_*/R)^{1/2}$. The relative velocity is assumed and is calculated from $v_r \sim \sqrt{v_p^2 + v_{d,K}^2}$. The solid, dashed, and dotted lines show the ratio of the shock distance and disk scale height at the pulsar for a base density of $\rho_0 = 10^{-9}\ \mathrm{g\ cm^{-3}}$, $10^{-10}\ \mathrm{g\ cm^{-3}}$ and $10^{-11}\ \mathrm{g\ cm^{-3}}$, respectively. The dashed–dotted line shows the ratio of the scale height and separation, H/a. A cavity in the pulsar wind around the pulsar may be formed when r_s/H is less than unity.

used $v_{d,K}(R_*) = 5 \times 10^7\ \mathrm{cm\ s^{-1}}$. The radial velocity of the disk matter, $v_{d,r} \sim 0.1c_s \sim 10^5\ \mathrm{cm\ s^{-1}}$ with $c_s \sim 10\ \mathrm{km\ s^{-1}}$ being the sound speed (Okazaki et al. 2011), is much slower than the pulsar motion and the disk's circular motion. Hence, by assuming the relative velocity $v_r \sim \sqrt{v_p^2 + v_{d,K}^2}$, the shock distance calculated from Equation (10) is $r_s \sim 10^{12}\ \mathrm{cm}(\rho_0/10^{-10}\ \mathrm{g\ cm^{-3}})^{-1/2}$ at periastron. A pulsar/Be disk interaction may cause a cavity in the wind around the pulsar, provided $r_s/H(a) \leqslant 1$, which yields $\rho_0 \geqslant 10^{-10}\ \mathrm{g\ cm^{-3}}$.

Figure 6 summarizes the ratio of the shock distance given by Equation (10) and the scale height of the disk, provided the pulsar interacts with the disk at the given orbital phase in the horizontal axis. The figure summarizes the shock distance for the epoch between −100 days and +100 days from periastron. The different lines show the case for a base density of $\rho_0 = 10^{-9}\ \mathrm{erg\ cm^{-3}}$ (solid line), $10^{-10}\ \mathrm{erg\ cm^{-3}}$ (dashed line) and $10^{-11}\ \mathrm{erg\ cm^{-3}}$ (dotted line), respectively. We find from the figure that a cavity will form ($r_s/H < 1$) at the periastron passage if $\rho_0 > 10^{-10}\ \mathrm{erg\ cm^{-3}}$. If the base density is less than $\rho_0 < 10^{-10}\ \mathrm{erg\ cm^{-3}}$, on the other hand, the pulsar wind will strip off an outer part of the Be disk, truncating it at a radius smaller than the pulsar orbit, and the pulsar wind/Be disk interactions will not affect the observed emission.

3.3. Shock Emissions

We calculate the emissions from the shock due to the interaction between the pulsar wind and stellar wind, as follows. The magnetic field at the shock radius but before the shock is calculated from

$$B_1 = \sqrt{\frac{L_{\rm sd}\sigma_0}{r_s^2 c(1+\sigma_0)}}, \tag{11}$$

where we defined $\sigma_0 \equiv \sigma(r_s)$. At the shock, the kinetic energy of the pulsar wind is converted into the internal energy of the shocked pulsar wind. Applying a jump condition of a perpendicular magnetohydrodynamic shock, we calculate the velocity $v_{pw,2}$, the magnetic field B_2, and the gas pressure P_2 of the shocked pulsar wind at the shock (Kennel & Coroniti 1984). For the particle kinetic energy dominating the un-shocked flow, that is, for the low σ_0 regime, we obtain

$$v_{pw,2} \sim \frac{c}{3}\sqrt{\frac{1+9\sigma_0}{1+\sigma_0}}, \tag{12}$$

$$B_2 \sim 3B_1(1-4\sigma_0) \tag{13}$$

and

$$P_2 \sim \frac{2(1-2\sigma_0)}{3(1+9\sigma_0)^{1/2}(1+\sigma_0)}\frac{L_{\rm sd}}{4\pi r_s^2 c}. \tag{14}$$

We assume that the post-shock pulsar wind flows along the shock surface. Along the downstream flow, we assume a conservation of the magnetic flux $B(r) = r_s B_2/r$. For the spherical symmetric flow, the bulk velocity decreases with distance from the shock (Kennel & Coroniti 1984). However, numerical simulations imply that the post-shock bulk flow for binary systems does not simply decrease but increases with distance from the shock, because of a rapid expansion of the flow in the downstream region (Bogovalov et al. 2008). Furthermore, the high-energy emissions take place in the vicinity of the shock radius. In this study, therefore, we assume the velocity field of the post-shock pulsar wind with $v_{\rm pw}(r) =$ constant.

We assume that the electrons and positrons in the pulsar wind are accelerated by the shock and form a power-law distribution over several decays in energy;

$$f_0(\gamma) = K_0\gamma^{-p}, \quad \Gamma_{\rm PW,0} \leqslant \gamma \leqslant \gamma_{\rm max}, \tag{15}$$

where we assume that the minimum Lorentz factor of the accelerated particles is equal to the average Lorentz factor of the particles forming the cold-relativistic pulsar wind (Section 3.4). We assume the maximum Lorentz factor by balancing between the acceleration timescale $\sim \gamma_{\rm max} m_e c/(\xi e B_2)$ and the synchrotron loss timescale $\sim 9m_e^3c^5/(4e^4B_2^2\gamma_{\rm max})$, yielding $\gamma_{\rm max} = [9\xi m_e^2c^4/(4e^3B_2)]^{1/2}$, where ξ represents the efficiency of the acceleration, which will be $\xi \leqslant 1$. The efficiency of the acceleration in gamma-ray binaries has been explained from the observed spectra of very high-energy emissions; for example, a high efficiency is required to explain the TeV emission of LS 5039 (Zabalza et al. 2013). For PSR J2032+4127/MT91 213, it is difficult to discuss efficiency, since TeV emission from this source has not yet been detected. In the calculations, we found that the predicted X-ray flux and 0.1–10 TeV flux are insensitive to the efficiency if $\xi > 10^{-4}$. In this study, therefore, we present the results with $\xi = 1$. Future TeV observations at the periastron passage may provide addition information constraining the efficiency.

For the injected particles at the shock, we assume $p = 2$ for the power-law index of the distribution. Since the particle energy density ϵ is related with the pressure P_2 as $P_2 = \epsilon/3$,

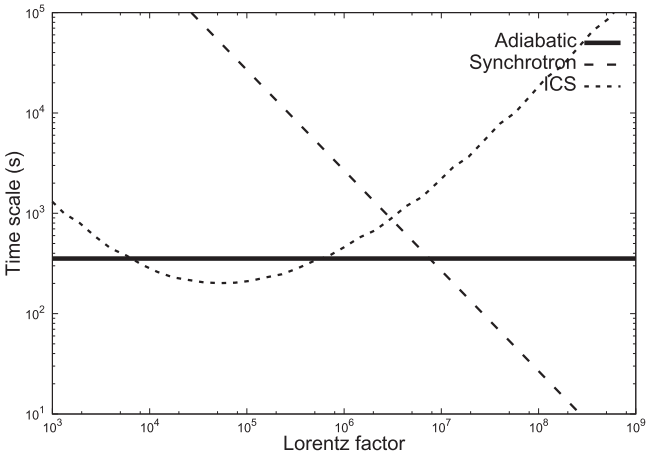

Figure 7. Cooling timescale as a function of the Lorentz factor at periastron and at the apex of the shock cone with $\eta = 0.085$. The magnetization parameter is $\sigma_0 = 0.1$ ($B_2 \sim 0.3$G). The solid, dashed, and dotted lines are timescale of the adiabatic cooling, synchrotron cooling, and ICS cooling, respectively.

the normalization factor K_0 of Equation (15) is calculated from the relation $P_2 = m_e c^2 \int_{\gamma_{\rm min}}^{\gamma_{\rm max}} \gamma f_0(\gamma) d\gamma / 3$.

We solve the evolution of the Lorentz factor after the shock with a simple one-dimensional treatment, that is,

$$\frac{d\gamma_e}{dr} = \frac{1}{v_{\rm pw}}\left[\left(\frac{d\gamma}{dt}\right)_{\rm ad} + \left(\frac{d\gamma}{dt}\right)_{\rm syn} + \left(\frac{d\gamma}{dt}\right)_{\rm ICS}\right]. \quad (16)$$

We assume the adiabatic loss given by

$$\left(\frac{d\gamma}{dt}\right)_{\rm ad} = \frac{\gamma}{3n}\frac{dn}{dt} = -\frac{2\gamma v_{\rm pm}}{3r},$$

where $n \propto r^{-2}$ is the particle number density. The synchrotron loss is given as

$$\left(\frac{d\gamma}{dt}\right)_{\rm syn} = -\frac{4e^2B^2\gamma^2}{9m_e^3c^5}. \quad (17)$$

We calculate the ICS energy loss rate using

$$\left(\frac{d\gamma}{dt}\right)_{\rm ICS} = -\int\int (E - E_s)\frac{\sigma_{\rm ICS}c}{m_e c^2 E_s}\frac{dN_s}{dE_s}dE_s dE, \quad (18)$$

where dN_s/dE_s is the stellar photon field distribution and $\sigma_{\rm ICS}$ is the cross-section with the isotropic photon field. For the soft-photon field, we consider the blackbody radiation from the B star and apply the Planck function with temperature $T_s = 30{,}000$ K, which is the case for the companion star of PSR B1259–63 (Negueruela et al. 2011). Figure 7 summarizes the timescale of the cooling at periastron and at the apex of the shock cone.

The TeV gamma-ray produced by the ICS process may be converted into an electron–positron pair through the photon–photon pair-creation process with the stellar photon. The cross section of this process is calculated from

$$\sigma_{\gamma\gamma}(E_s, E_\gamma) = \frac{3}{16}\sigma_T(1 - v^2)\left[(3 - v^4)\ln\frac{1+v}{1-v} - 2v(2 - v^2)\right], \quad (19)$$

where

$$v(E_s, E_\gamma) = \sqrt{1 - \frac{2}{1 - \cos\theta_{\gamma\gamma}}\frac{(m_e c^2)^2}{E_s E_\gamma}},$$

where $\theta_{\gamma\gamma}$ is the collision angle between the soft photon and gamma-ray, and is a function of position. The optical depth is calculated from $\tau(E_\gamma) = \int\int \sigma_{\gamma\gamma}(E_s, E_\gamma) n_s(E_s) dE_s d\ell$, where $n_s(E_s)$ represents the energy distribution of the stellar radiation number density (see Table 1 for the parameters of the companion star). Figure 8 summarizes the optical depth of the high-energy photons emitted from the shock apex ($\eta = 0.085$); different lines in the figure represent difference system inclination angles θ_E and different positions of the pulsars along the orbit. We find in Figure 8 that the optical depth of the 0.1–1TeV photons emitted around periastron and the SUPC exceeds unity, indicating the TeV photons emitted during the periastron passage are significantly absorbed by the stellar photons.

3.4. ICS Process of the Cold-relativistic Pulsar Wind

The pulsar binaries will be a laboratory to search for evidence of the high-energy gamma-rays produced by the ICS process of the cold-relativistic pulsar wind (Cerutti et al. 2008). In this study, we assume the pulsar wind is isotropic and is formed near the light cylinder of the pulsar, which is $r_{\rm lc} \sim 6.8 \times 10^8$ cm for PSR J2032+4127. Since there is a theoretical uncertainty in the particle distribution of the cold-relativistic pulsar wind, we explore the process with a relativistic Maxwell distribution of the form,

$$f(\Gamma_{\rm PW}) \propto \Gamma_{\rm PW}^2 \exp\left(-\frac{3\Gamma_{\rm PW}}{\Gamma_{\rm PW,0}}\right), \quad (20)$$

which provides an average Lorentz factor of $\sim\Gamma_{\rm PW,0}$. The normalization is calculated from the condition that

$$m_e c^2 \int_0^\infty \Gamma_{\rm PW} f(\Gamma_{\rm PW}) d\Gamma_{\rm PW} = \frac{L_{\rm sd}}{4\pi r^2 c(1 + \sigma)}. \quad (21)$$

Due to the unknown energy conversion process from magnetic energy to particle energy, the magnetization parameter will evolve with radial distance from the pulsar. From the energy conservation, the average Lorentz factor of the cold-relativistic pulsar wind just before the shock may be described as $\Gamma_{\rm PW,0}(r_s) = \Gamma_L(1 + \sigma_L)/[1 + \sigma_0]$, which provides $\Gamma_{\rm PW,0}(r_s) \sim \Gamma_L\sigma_L$ in the limit of $\sigma_L \gg 1$ and $\sigma_0 \ll 1$, where Γ_L and σ_L are the Lorentz factor and the magnetization parameter at the light cylinder, respectively. The pairs created inside the light cylinder lose their momentum perpendicular to the magnetic field line via synchrotron radiation, and they will eventually escape from the light cylinder with a Lorentz factor of $\Gamma_L \sim 10$. Hence, the magnetization parameter at the light cylinder may be estimated from

$$\sigma_L = \frac{B_L^2}{4\pi\Gamma_L\kappa n_{GJ,L} m_e c^2} \sim 9 \times 10^2 \left(\frac{\Gamma_L}{10}\right)^{-1}\left(\frac{\kappa}{10^5}\right)^{-1} \quad (22)$$

where κ is the multiplicity and we applied $P = 0.143$s and $B_L = 4.3 \times 10^3$G of PSR J2032+4127. From observations of pulsar wind nebulae, the multiplicity is expected to be $\kappa \sim 10^{5-6}$

Table 1
Parameters of the Binary Systems

PSR/Companion	P (s)	L_{35}	P_o (years)	e	a (lt-s)	T_*	R_*
J2032+4127/MT91 213	0.143	1.7	25–50	0.96	9022	30,000 K	$10R_\odot$
B1259–63/LS2883	0.048	8	3.4	0.83	1296	∼30,000 K	$\sim 9R_\odot$

Note. P: spin period of the pulsars. L_{35}: spin-down luminosity in units of 10^{35} erg cm^{-2} s^{-1}. P_o: orbital period. e: eccentricity. a: projected semimajor axis. T_*: surface temperature of companion star. R_*: radius of B star. T_* and R_* of MT91 213 represent the values used in the calculation. References: Ho et al. (2017) for J2032+3127 and Negueruela et al. (2011) for B1259–63.

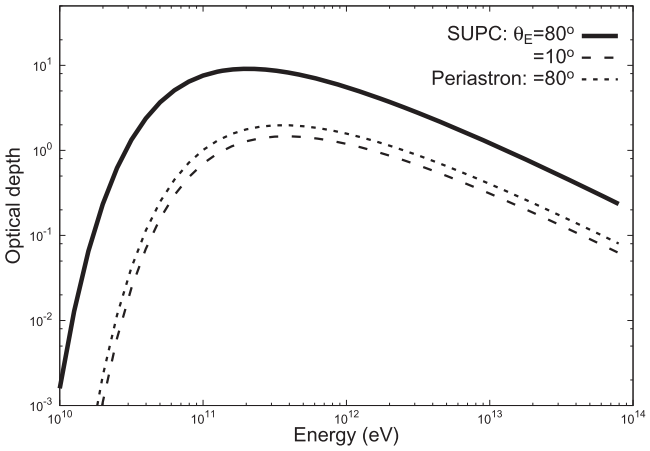

Figure 8. The optical depth of the photon–photon pair-creation process as a function of the energy of the photon propagating toward the observer. The solid and dashed lines show the optical depth at the SUPC with assumed system inclination angle $\theta_E = 10°$ and 80°, respectively. The dotted line is the optical depth at periastron with $\theta_E = 80°$. The anomaly of the direction of Earth is $\phi_E = 230°$.

for Crab-like young pulsars (Tanaka & Takahara 2010) and $\kappa \sim 10^{2-3}$ for Vela-like pulsars (Sefako & de Jager 2003). Theoretical studies have implied a multiplicity $\kappa \sim 10^{2-5}$ (Hibschman & Arons 2001; Timokhin & Harding 2015). Hence we assume the typical value of the Lorentz factor of the pulsar wind is in the range of $\Gamma_{\rm PW,0} \sim \Gamma_L \sigma_L \sim 10^{3-6}$.

The power per unit energy per unit solid angle of the ICS process with an anisotropic soft-photon field may be calculated from

$$\frac{dP_{\rm ICS}}{d\Omega} = \mathcal{D}_{\rm ICS} \int (1 - \beta \cos\theta_0) I_b / h \frac{d\sigma'_{\rm ICS}}{d\Omega'} d\Omega_*, \qquad (23)$$

where $d\Omega_*$ is the solid angle of the sky covered by the B star measured from the emission region, $\mathcal{D}_{\rm ICS} = \Gamma^{-1}(1 - \beta \cos\theta_1)^{-1}$ with θ_1 (or θ_0) describing the angle between the direction of the particle motion and the propagating direction of the scattered photons (or background photons). In addition, I_b is the Planck function of the stellar photon field, and $d\sigma'_{\rm ICS}/d\Omega'$ is the differential Klein–Nishina cross section.

Figure 9 shows the expected light curves (left panel) and spectra at periastron (right panel) for the different system inclination angles relative to the Earth viewing angle (θ_E) and the average Lorentz factor of the pulsar wind $\Gamma_{\rm PW,0}$, respectively. As the left panel indicates, the calculated emissions for a larger viewing angle are suppressed at around −150 days from periastron. This is because the INFC occurs at ∼−150 days from periastron (Figure 2), and because around the INFC the ICS process between a soft photon from the B star and a pulsar wind particle moving toward the Earth is a tail-on collision process, which reduces the ICS efficiency. Since the SUPC is ∼+10 days after periastron, the calculated flux measured from the Earth becomes maximum around, but after, periastron. As the right panel shows, the energy flux in the GeV energy bands is $\sim 10^{-10}$ erg cm^{-2} s^{-1} for $\Gamma_{\rm PW,0} \sim 10^{4-5}$, which is close to the observed flux level ($\sim 2 \times 10^{-10}$ erg cm^{-2} s^{-1}) of the pulsed emission from *Fermi*-LAT. Hence, we expect that if $\Gamma_{\rm PW,0} \sim 10^{4-5}$, *Fermi*-LAT will observe an increase in the GeV flux during the next periastron passage.

4. Model Results

In the current calculation, we applied the system parameters suggested by Ho et al. (2017), namely, the orbital period of $P_{\rm ob}$= 17,000 days, and the anomaly of the direction of the Earth $\phi_E \sim 230°$ (Figure 2). In addition, we apply $d = 1.5$ kpc (Lyne et al. 2015) and MJD 58069 as the periastron. We have not presented the results of the calculations for the orbital phase <−4000 days and >+4000 days from periastron, since we are interested in the emission processes around it. We note that within the current uncertainties of the orbit parameters ($P_{\rm ob}$, e) ∼ 25 yr, 0.93 in Lyne et al. (2015) and 50 yr, 0.96 given by Ho et al. (2017), the main conclusions of the model results are not affected, since the system sizes predicted by these two groups are very similar to each other.

4.1. X-ray/TeV Emissions

As described in the previous section, *Swift* observed a rapid increase in the emissions in the 0.3–10 keV energy bands after ∼MJD56250 (see Figure 3). These X-ray emissions are probably a result of the pulsar wind/stellar wind interaction, since the pulsar/Be disk interaction will be important only around periastron (say, between −100 days and +100 days), as discussed in Section 3.2. In this section, therefore, we will discuss the X-ray and TeV emissions from the shock caused by the pulsar wind and stellar wind interaction, and will examine the pulsar wind properties by comparing the model results with the observed X-ray light curve.

4.1.1. Constant σ

First, we consider the case where the magnetization parameter is constant with the radial distance from the pulsar, namely, the magnetization parameter at the shock does not depend on the shock distance. We also ignore the Doppler boosting effect caused by the finite velocity of the shocked pulsar wind, which will be discussed in Section 4.1.2. Figure 10 summarizes the calculated flux and orbital modulation in the 0.3–10 keV energy bands (left panel) and in the 0.1–10 TeV energy bands (right panel); the solid, dashed, and dotted lines are for $\sigma_0 = 0.5$, 0.1, and 0.01, respectively. In the calculation, we assumed $\eta = 0.085$ (that is, $\dot{M}_W \sim 10^{-8} M_\odot$ yr^{-1}), and

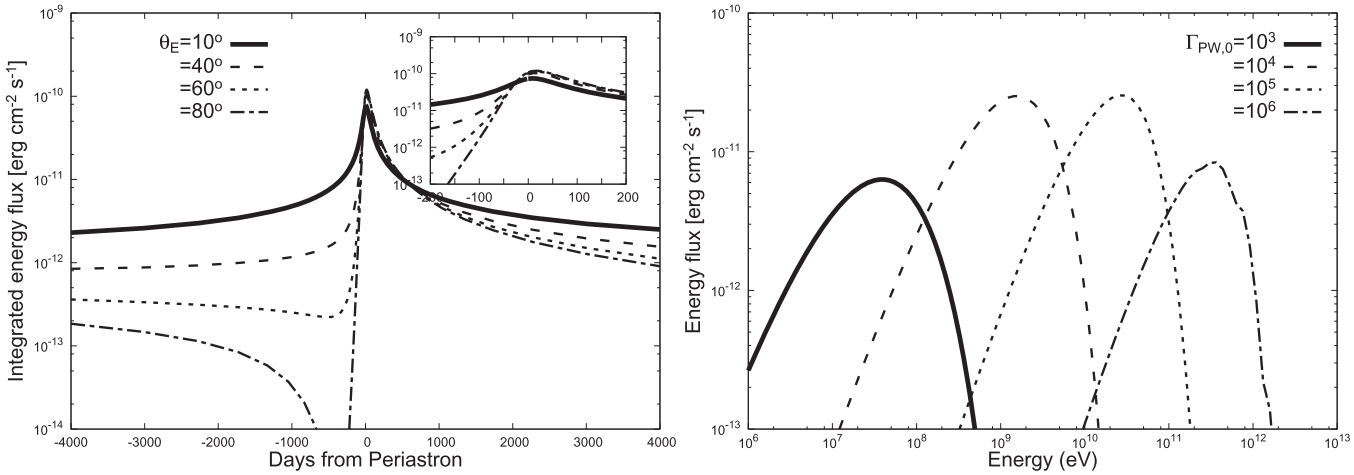

Figure 9. The orbital modulations (left panel) and the spectra (right panel) of the ICS process between the cold-relativistic pulsar wind and stellar photons. Left: the orbital modulations for the different observing angle (θ_E) measured from the direction perpendicular to the orbital plane. The results are for $\Gamma_{\rm PW,0} = 10^4$. Right panel: the calculated spectra at periastron. The results are for $\theta_E = 60^\circ$.

$\Gamma_{\rm PW,0} = 10^4$. In the left panel of the figure, the results of the *Swift* observations are also displayed.

We find in Figure 10 that the calculated light curve with constant magnetization parameter predicts an increase in the X-ray flux slower than that of the *Swift* observations after ~ -2000 days from periastron. The synchrotron luminosity is roughly proportional to $L_{\rm syn} \propto r_s B^2(r_s) \propto 1/r_s$ for a constant magnetization parameter. As Figure 5 shows, the shock distance decreases by about a factor of $\sim$2 during ~ -2000 days and ~ -1000 days, and therefore, the calculated flux slightly increases during that epoch, which cannot explain the increase in the flux (a factor of $\sim$5–10) measured by *Swift*.

Figure 11 shows how the calculated flux depends on the model parameters, namely, the magnetization parameter (left panel) and the average Lorentz factor of the un-shocked pulsar wind $\Gamma_{\rm PW,0}$ (right panel). As seen in the left panel, the calculated X-ray flux (solid line) reaches its maximum value at the magnetization parameter $\sigma_0 \sim 0.1$. This is because the internal energy ($\propto P_2$) of the post-shock flow at the shock given by the jump condition decreases as the assumed magnetization parameter increases (e.g., Figure 4 of Kennel & Coroniti 1984), while the magnetic field at the shock (B_2) increases as the magnetization parameter increases. The former tends to decrease the calculated X-ray flux, while the latter increases it. These two effects compensate each other and the calculated X-ray flux becomes maximum at the magnetization parameter $\sigma_0 \sim 0.1$. We find therefore that it is difficult to explain the observed X-ray flux of *Swift* after ~ -1000 days using the magnetization parameter $\sigma_0 \sim 1$. By comparing the calculated flux and *Swift* observations, therefore, we conclude that the magnetization parameters at the shock is of order of $\sigma_0 \sim 0.1$ at ~ -1000 days. It is possible that the Lorentz factor $\Gamma_{\rm PW,0}$ of the cold-relativistic pulsar wind evolves with the shock distance from the pulsar. In the right panel, however, we can see that the calculated fluxes in X-ray/TeV energy bands are less dependent on the minimum Lorentz factor of the shocked particles at the shock ($\Gamma_{\rm PW,0}$).

In the calculated TeV light curve (right panel in Figure 10), we can see an asymmetry relative to the periastron. Since the TeV photons from the shock are produced by the ICS process, the asymmetry is introduced by the dependence of the collision angle between the stellar photons and the shocked pulsar wind particles that emit the photons toward the Earth, as in the case with the orbital modulation of the ICS of the cold-relativistic pulsar wind (Figure 9).

For the TeV photons, the optical depth of the pair-creation process depends on the orbital phase, and it becomes maximum at the SUPC for photons traveling toward the Earth. This effect can be seen as a rapid drop in the calculated flux around $\sim +10$ days. The calculated TeV emission from the shock depends on the Earth viewing angle, as summarized in Figure 12.

4.1.2. Doppler Boosting Effect

In the previous sections, we ignored the effect of the motion of the post-shocked pulsar wind. In such a case, as Figure 10 indicates, the orbital modulation of the X-ray emission is symmetric relative to the periastron. Asymmetry in the X-ray light curve as well as in the TeV light curve will be introduced by the finite velocity of the shocked pulsar wind.

The finite velocity of the shocked pulsar wind will cause the Doppler boosting effect, which enhances or suppresses the observed emissions. It has been suggested that the observed modulation of the X-ray emissions from LS 5039 is a result of this effect (Dubus et al. 2010; Takata et al. 2014a). The Doppler factor is calculated from

$$\mathcal{D} = \frac{1}{\Gamma_{\rm pw}\sqrt{1 - (v_{\rm pw}/c)\cos\theta_{\rm pw}}}, \tag{24}$$

where $\Gamma_{\rm pw}$ is the Lorentz factor of the bulk motion of the post-shocked flow, and $\theta_{\rm pw}$ is the angle of the flow direction and the line of sight. We assume that the velocity of the post-shocked pulsar wind flow is constant.

Figure 13 summarizes the Doppler boosting effect with different velocities of the post-shocked flow, $v_{\rm pw} = v_{pw,2}$ (solid lines) given by the jump condition, $c/3$ (dashed line) in the limit of $\sigma_0 = 0$, and $0.6c$ (dotted line). We can see that the Doppler boosting effect enhances the emissions before periastron, while suppressing after it. With $\eta < 1$, namely for the stellar wind stronger than the pulsar wind, the shock-cone wraps around the pulsar. Around the INFC (~ -150 days), the

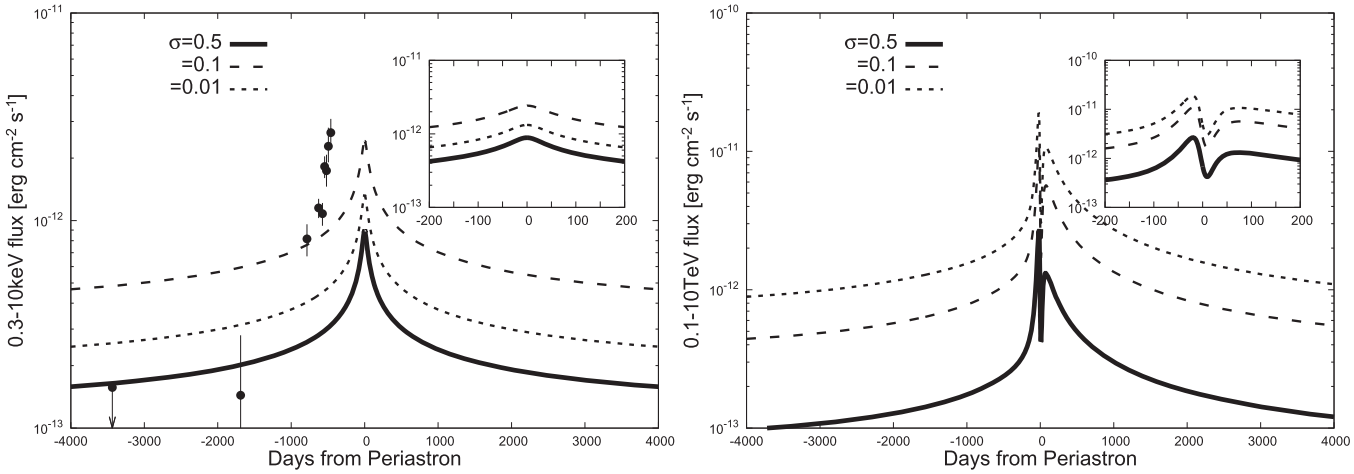

Figure 10. Modulation in the 0.3–10 keV energy bands (left panel) and in the >1TeV energy bands (right panel) with constant magnetization parameter. The solid, dashed, and dotted lines are results for $\sigma_0 = 0.5$, 0.1, and 0.01,respectively. The sub-panel enlarges the modulation between −100 days and 100 days from periastron. The results are for $\Gamma_{\rm PW,0} = 10^4$, $\eta = 0.085$ and $\theta_E = 60°$.

post-shocked pulsar wind moves toward the Earth and hence enhances the emissions. These are suppressed around the SUPC (∼+10 days) where the post-shocked pulsar wind moves away from the Earth. However, the Doppler boosting effect will not be the reason for the rapid increase in the X-ray emissions observed by *Swift*.

4.1.3. Dependence on Wind Momentum Ratio

It has been considered that mass loss from the companion star will be driven by the radiation pressure, and the rapidly rotating main-sequence star, such that the angular velocity of the star rotation is close to its Keplerian angular velocity, and produces a stellar wind enhanced in the polar region (Georgy et al. 2011 and references therein). It is also considered that anisotropy of the pulsar wind explains the torus-like and jet-like structures of the pulsar wind nebulae, and theoretical models suggest that angular distribution of the pulsar wind energy is proportional to $\sin^2\theta$, where θ is the angle measured from the spin axis (Bogovalov & Khangoulian 2002). The anisotropy of the two winds could change the momentum ratio η at their interaction region along the orbit.

Besides the large structure of the anisotropy, an irregularity of the stellar wind from the high-mass star could be formed. It has been discussed that a radiatively non-stationary acceleration process produces clumping (small-scale density inhomogeneity) of the stellar wind from the high-mass star (Runacres & Owocki 2002; Owocki & Cohen 2006). It was analyzed that the typical size of a clump at the stellar surface is $\sim 0.01 R_*$, and may linearly expand with radial distance. A larger structure of clumps could be formed in the wind due to difference production mechanisms, magnetic field inhomogeneities, and the star's rotation/pulsation (see Bosch-Ramon 2013). Although the clumps fill only a small fraction of the volume of the wind region, it is thought that they carry most of mass ejected from the star, and have a mass density larger than the average density of the wind. Studies with hydrodynamic simulations have shown that the clumping could develop in size and mass density due to merging between dense shells traveling from the star, although it was also pointed out that break-up of the dense shell as a consequence of the Rayleigh–Taylor or thin-shell instability limits the clump growth (Bozzo et al. 2016, and references therein). If a clumpy wind is formed in a high-mass binary system hosting a compact object, it is expected that the irregularity of the mass density in the stellar wind will cause a temporal evolution of the momentum ratio (η), yielding temporal variations in the shock emissions (Owocki et al. 2009; Bosch-Ramon 2013; de la Cita et al. 2017).

The calculated X-ray fluxes depend on the wind momentum ratio, which determines the location of the shock. Figure 14 shows the calculated light curves for $\eta = 0.85$ (solid lines), 0.085 (dashed lines), and 0.0085 (dotted lines), respectively, with parameters $\sigma_0 = 0.1$ and $\Gamma_{\rm PW,0} = 10^4$. As we can see, the calculated X-ray flux increases with decreasing momentum ratio, because the shock distance from the pulsar decreases and hence the magnetic field at the shock increases with decreasing momentum ratio. As the figure shows, a decrease in the momentum ratio (that is, the stellar wind becomes stronger relative to the pulsar wind) by a factor of ten can give an increase in the observed X-ray fluxes during ∼−2000 days to ∼−1000 days from periastron. Such momentum evolution with time could be caused by the anisotropy of the stellar wind/pulsar wind. A shorter timescale variability will be also possible as a consequence of the pulsar wind/clumpy wind interaction.

The observed flux ratio between the X-ray and TeV energy bands may provide additional information for the magnetization parameter and momentum ratio of the pulsar wind to the stellar wind. As we expect, the flux ratio of X-ray and TeV does not greatly depend on $\Gamma_{\rm PW,0}$, but it is sensitive to the energy densities of the magnetic field and soft-photon field at the emission region, which mainly depends on the magnetization parameter and the momentum ratio of the two winds. Figure 15 presents the dependence of $F_{0.3-10\,\rm keV}/F_{0.1-10\,\rm TeV}$ on the magnetization parameter and the wind momentum ratio. If future observations could measure the flux ratio in the X-ray and TeV energy bands, we could discuss the momentum ratio of the two winds; for example, if future observations provide $F_{0.3-10\,\rm keV}/F_{0.1-10\,\rm TeV} \sim 1$ at periastron, the current model predicts that the magnetization $\sigma_0 \sim 1$ if the momentum ratio $\eta \sim 0.0085$.

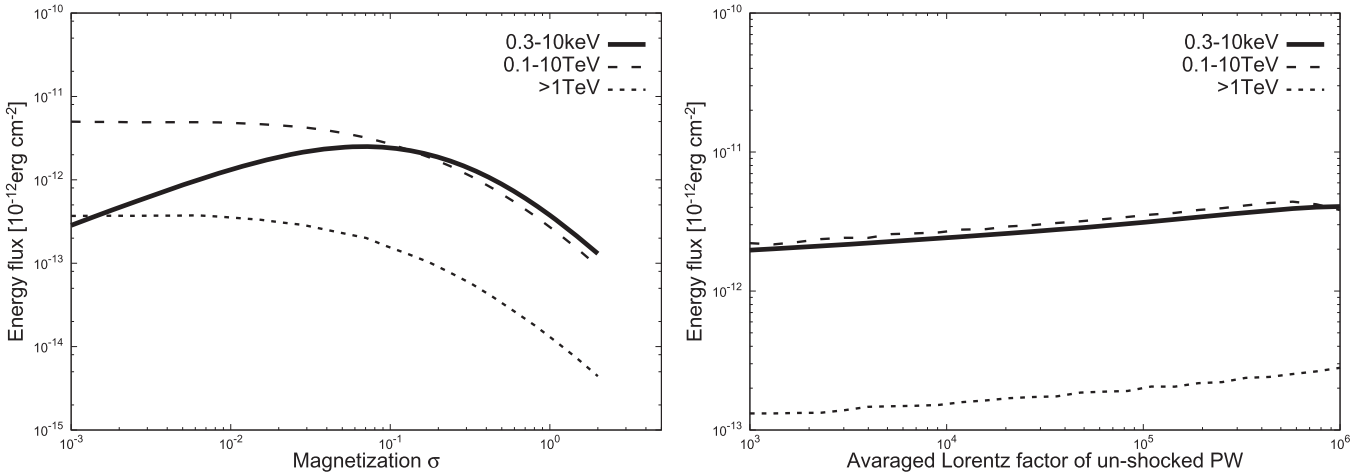

Figure 11. Dependence of the calculated X-ray (solid line) and TeV (dashed line) as a function of the magnetization parameter with $\Gamma_{\rm PW,0} = 10^4$ (left panel) and Lorentz factor (right panel) with $\sigma_0 = 0.1$. The results are for the periastron and $\theta_E = 60^\circ$.

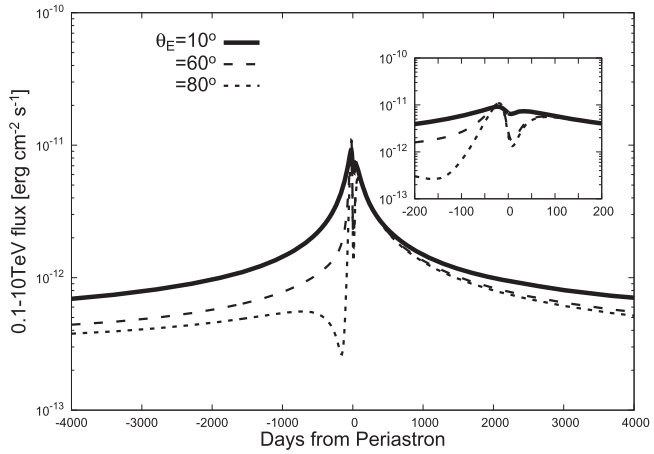

Figure 12. Dependence of the calculated 0.1–10 TeV light curve on the Earth viewing angle measured from the direction perpendicular to the orbital plane. The solid, dashed, and dotted lines are for $\theta_E = 10^\circ$, 60°, and 80°, respectively. In addition, $\sigma_0 = 0.1$ and $\Gamma_{\rm PW,0} = 10^4$.

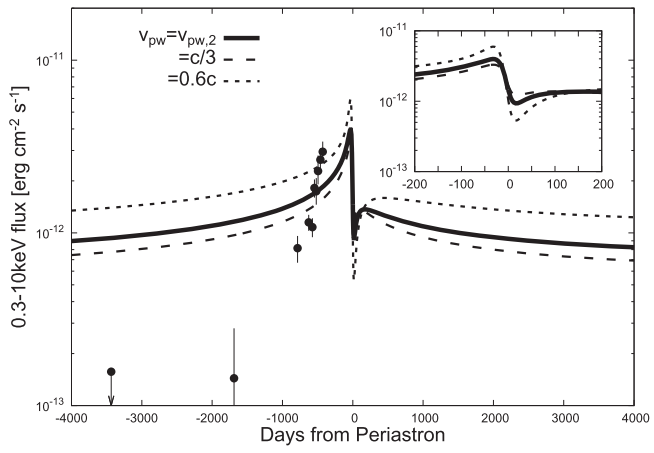

Figure 13. Orbital modulation with Doppler boosting effect due to the finite velocity of the shocked pulsar wind. The different lines assume different flow velocities; $v_{\rm pw} = v_{pw,2}$ (solid line) given by the jump condition, $c/3$ (dashed line), and $0.6c$ (dotted line), respectively. The assumed inclination angle of the system is $\theta_E = 60^\circ$. The results are for $\eta = 0.085$, $\Gamma_{\rm PW,0} = 10^4$, and $\sigma_0 = 0.1$.

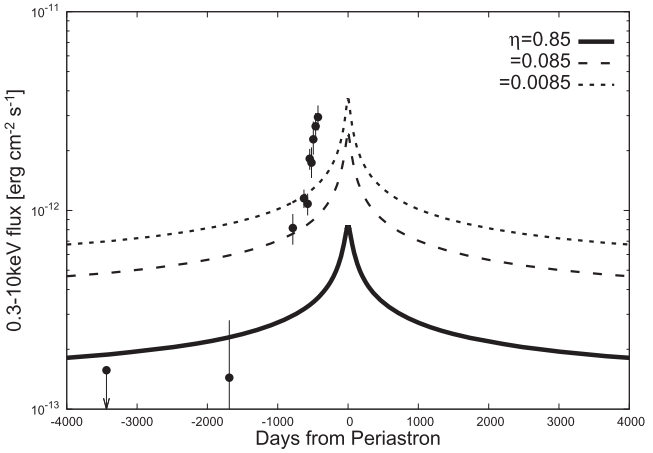

Figure 14. The expected orbital X-ray modulations with different momentum ratios of the pulsar wind and stellar wind; $\eta = 0.85$ for the solid line, 0.085 for the dashed line, and 0.0085 for the dotted line. The results are for $\sigma_0 = 0.1$, $\Gamma_{\rm PW,0} = 10^4$ and $\theta_E = 60^\circ$.

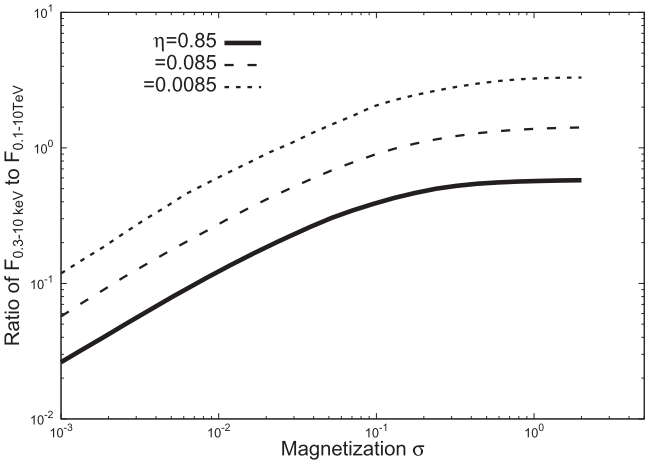

Figure 15. The calculated ratio of the X-ray and TeV flux at periastron as a function of the magnetization parameter. The results are for the momentum ratio of the two winds $\eta = 0.0085$ for the solid line, 0.085 for the dashed line, and 0.85 for the dotted line. In addition, $\Gamma_{\rm PW,0} = 10^4$ and $\theta_E = 60^\circ$.

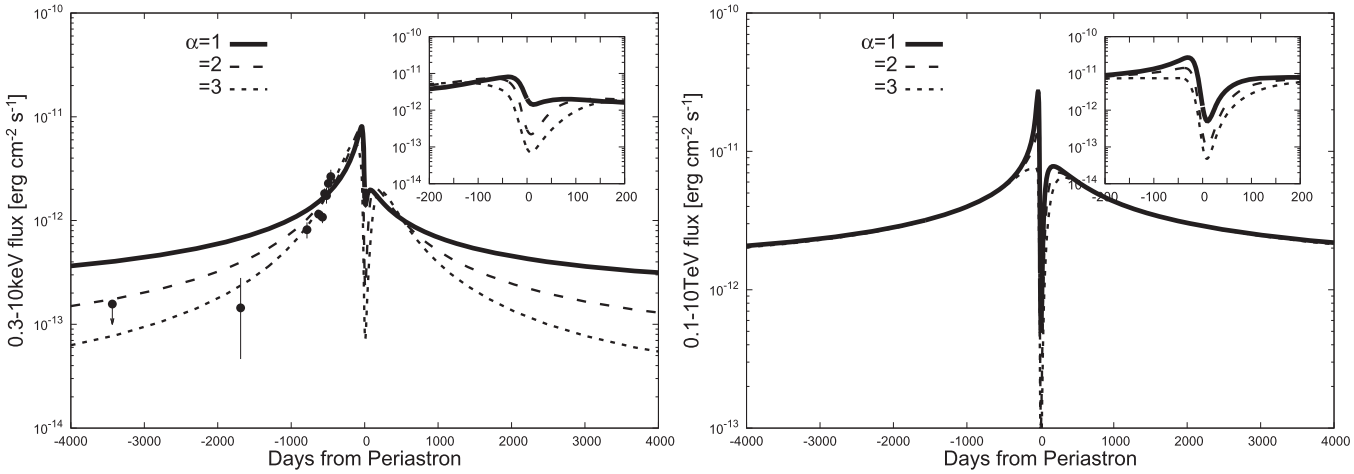

Figure 16. The X-ray (left) and TeV (right) light curves with a radial-dependent magnetization parameter. The solid, dashed, and dotted lines are results for $\alpha = 1$, 2, and 3, respectively in Equation (25). All cases assume $\eta = 0.02$ and $\Gamma_{\rm PW,0} = 10^4$. The magnetization parameter for each case is normalized to be $\sigma \sim 0.01$ at $r \sim 2.5$ au.

4.1.4. Radial-dependent σ of the Pulsar Wind

As seen in Figures 10, 13, and 14, the calculated X-ray light curve cannot explain the *Swift* observations after ~ -2000 days, if the momentum ratio does not significantly change along the orbit. The radial-dependent magnetization parameter has been discussed in previous studies to explain the orbital modulations of gamma-ray binaries (Takata & Taam 2009; Takata et al. 2014a; Kong et al. 2011). In this paper, we explore the radial dependence with a function form of

$$\sigma(r) \propto r^{-\alpha}. \tag{25}$$

The left panel in Figure 16 shows the results of fitting the Swift X-ray data with different power law indices. Other parameters are $\eta = 0.02$ ($\dot{M} \sim 4 \times 10^{-8} M_\odot\,{\rm yr}^{-1}$) and $\Gamma_{\rm PW,0} = 10^4$. In addition, we applied $v_{\rm pw} = v_{pw,2}$ taking into account the Doppler boosting effect discussed in Section 4.1.2. To explain the observed flux level from *Swift*, we normalized the magnetization parameter to be $\sigma \sim 0.01$ at $r \sim 2.5$ au for each power law index. Figure 17 shows the evolution of the fitting magnetization parameters at the apex of the shock cone as a function of the orbital phase.

We can see in Figure 16 that a faster evolution (larger α) of the magnetization parameter with radial distance reproduces a X-ray light curve being more consistent with the *Swift* observations after -4000 days. As the figure shows, the current model predicts that the peaks of the flux in the light curve occur a day before periastron and the flux then rapidly decreases during ~ -20 days and $\sim +10$ days by about one order of magnitude. This is because (1) the assumed magnetization parameter determined by the relation, $\sigma(r) \propto r^{-\alpha}$, exceeds unity for $\alpha > 2$, as Figure 17 shows, and (2) the Doppler boosting suppresses the emissions around the SUPC. This feature can be tested by future observations.

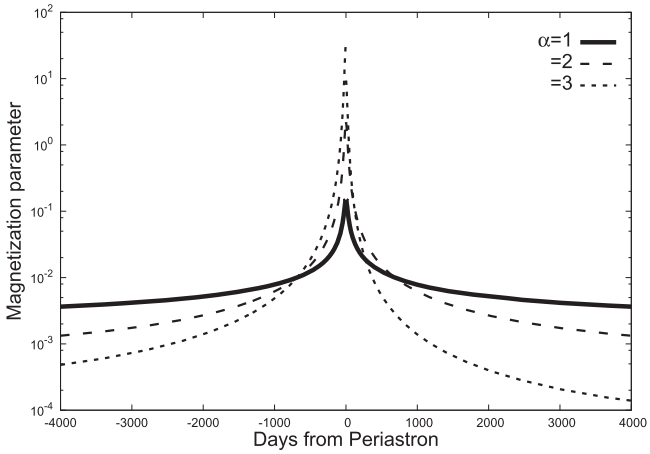

Figure 17. The value of the magnetization parameter at the shock-apex along the orbital phase. Model parameters for the lines are same as those in Figure 16.

4.2. GeV Emissions and Multi-wavelength Spectra

Gamma-ray binaries have also been detected by *Fermi*-LAT and the emission will originate from the magnetospheric processes and/or the intra-binary processes. For PSR J2032 +4127, the pulsed GeV emission due to the pulsar spin has been measured by *Fermi*-LAT with an energy flux $\sim 1.6 \times 10^{-10}$ erg cm^{-2} s^{-1} (Section 2). The high-energy tail of the synchrotron spectrum and the low energy tail of the ICS process of the intra-binary shock discussed in the previous sections could contribute to the energy bands (0.1–300GeV) of *Fermi*-LAT. In addition to the shock emissions, the ICS process of the cold-relativistic pulsar wind with $\Gamma_{\rm PW,0} \sim 10^{4-5}$ produces GeV gamma-rays (Figure 9).

Figure 18 compares the observed flux level of the pulsed emissions with the predicted flux levels of the shocked emissions (solid line) and of the ICS process of the cold-relativistic pulsar wind (dashed line). In the calculation, we assume $\Gamma_0 = 10^4$ for the average Lorentz factor of the particles of the cold-relativistic pulsar wind, and $\theta_E = 60^\circ$ for the inclination of the system. As we see, the emissions from the intra-binary space are comparable to the magnetospheric emissions around periastron. With the current parameters, therefore, we expect that *Fermi*-LAT measures the orbital modulation of the GeV flux during the periastron passage that will occur in late 2017 or early 2018.

In Figure 19, we present the model broadband spectra averaged over -100 days to $+100$ days; the model parameters are $\alpha = 2$ in Equation (25), $\eta = 0.02$ and $v_{\rm pw} = v_{pw,2}$, which reproduce the observed X-ray light curves. To see the dependence of the Lorentz factor $\Gamma_{\rm PW,0}$, we calculated the

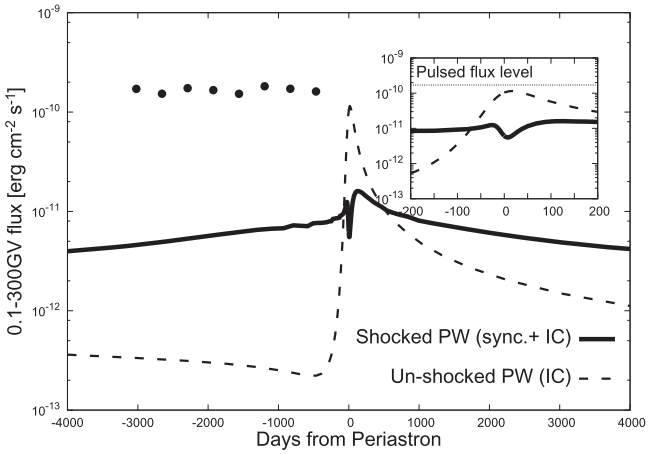

Figure 18. The orbital modulation of the calculated 0.1–100 GeV fluxes. The solid line and dashed line correspond to the emissions from the shocked pulsar wind and cold-relativistic pulsar (un-shocked pulsar wind), respectively. The shock emissions include the synchrotron radiation and ICS process of the shocked pulsar wind emissions. The eight-year *Fermi*-LAT data are also displayed. The results of the calculation are for $\Gamma_{\rm PW,0} = 10^4$, $\sigma_0 = 0.1$ and $\theta_E = 60^\circ$.

spectra for $\Gamma_{\rm PW} = 10^4$ (right panel) and 10^6 (left panel), respectively. The solid line shows the calculated spectrum combining the synchrotron and ICS process at the shock, and the dashed line represents the spectrum of the ICS process of the cold-relativistic pulsar wind. The current model predicts that the magnetospheric emissions dominate in the spectral energy distribution averaged over the periastron passage. If the minimum Lorentz factor of the shocked pulsar wind particles is $\Gamma_{\rm PW} \sim 10^6$, the TeV spectrum will show a turnover at around $\sim 10^{11}$eV and the X-ray spectrum has a break at around 10 keV.

5. Discussion and Summary

5.1. Emissions from the Secondary Pairs

During the periastron passage, the TeV photons from the shocked pulsar wind may be converted into pairs by the photon–photon pair creation process with the stellar photon fields; in particular, the TeV photons emitted toward the B star will be totally absorbed. These secondary pairs created in the stellar wind will also emit non-thermal photons via the synchrotron and ICS processes, and may initiate a further pair-creation cascade. If these pairs are isotropized, they will emit photons propagating toward the observer, even though the primary TeV photons do not do this (Bednarek 1997, 2007; Sierpowska & Bednarek 2005; Sierpowska-Bartosik & Bednarek, 2008; Sierpowska-Bartosik & Torres 2007, 2008; Cerutti et al. 2010; Yamaguchi & Takahara 2010).

The emissions from the secondary pairs produced in the stellar wind side will be dominated by the ICS process. The ratio of the radiation power between the synchrotron radiation and ICS processes will be described by the energy density ratio of the magnetic field to the stellar photon. The ICS process dominates the synchrotron radiation process at a radial distance from the star of

$$R \geqslant R_* \times 6.5^{\frac{1}{2(m-1)}} \left(\frac{B_*}{10^3\,{\rm G}}\right)^{\frac{1}{m-1}} \left(\frac{T_*}{30{,}000\,{\rm T}}\right)^{-\frac{2}{m-1}}, \quad (26)$$

where B_* represents the stellar magnetic field at the stellar surface. In addition, we assumed $B(R) \propto R^{-m}$ as the radial evolution of the stellar magnetic field. It is known that some high-mass main-sequence stars have a surface dipole magnetic field of order 10^3 G (Walder et al. 2012). With a typical value of $m = 2 \sim 3$, we can see that the synchrotron radiation of the created pairs in the stellar wind side can be important only very near the stellar surface and its contribution to the observed X-ray emissions will be negligible.

By tracing the primary TeV gamma-rays from all emission regions considered in the calculation box, we calculated the ICS process of the secondary pairs. We assumed that the pairs produced in the stellar wind side are quickly isotropized, and we calculated the emission process with a constant photon field during the crossing time, $\sim R_i/c$, where R_i represents the distance of the pair-creation position from the stellar surface. Figure 20 compares the spectra, which are measured on the Earth, of the ICS photons from the shock region (solid line) and from the secondary pairs (dashed line) at periastron, where we assumed that all photons from the secondary pairs can escape the pair-creation process. A further pair-creation cascade will make the spectra softer. As the figure shows, the integrated flux from the secondary pairs is much less than the primary emissions, and therefore we expect that the contribution of the emissions from higher-order pairs is much less than that from the shock emissions. The emissions from the secondary pairs could contribute to the 0.1–1 TeV bands, where the shock emissions around the periastron are significantly absorbed.

5.2. Pulsar/Be Disk Interaction

The interaction of PSR J203+4127 and the Be disk of MT91 213 may enhance the high-energy emissions, as in the case with the PSR B1259–69/LS2883 system showing an increase in the X-ray/TeV fluxes at the pulsar/Be disk interaction phase (Chernyakova et al. 2006). As we discussed in Section 3.2, we expect that the pulsar/Be disk interaction in this system affects the observed emissions, provided that the base density is $\rho_0 > 10^{-10}$ g cm^{-3} and the interaction occurs at the periastron passage, say between -100 days and $+100$ days from periastron (Figure 6). Since we do not know the geometry (e.g., inclination relative to the orbital plane) of the disk, we cannot predict when the pulsar interacts with it. We expect however that the pulsar/Be disk interaction will occur at least once during the periastron passage during -100 days and $+100$ days, since the true anomaly $\pm 90^\circ$ corresponds to $\sim \pm 50$ days from periastron.

If the base density of the Be disk is close to $\rho_0 \sim 10^{-9}$ g cm^{-3}, an interaction between pulsar and Be disk at the periastron passage will form a cavity in the pulsar wind, and most of the pulsar wind (4π sr in solid angle) will be stopped at the radial distance from the pulsar given by Equation (10) and Figure 6. In Figure 21, we show an example of the calculated light curve for pulsar/Be disk interactions and compare the estimated X-ray/TeV fluxes with those for the latter interactions. For the calculation, we assumed a base density $\rho_0 = 10^{-9}$ g cm^{-3}, magnetization $\sigma_0 = 0.1$, and momentum ratio $\eta = 0.085$ for the pulsar wind/stellar wind interaction.

Figure 21 indicates that the pulsar/Be disk interaction predicts X-ray fluxes several factors larger than those due to the pulsar/Be wind interaction, if the magnetization parameter

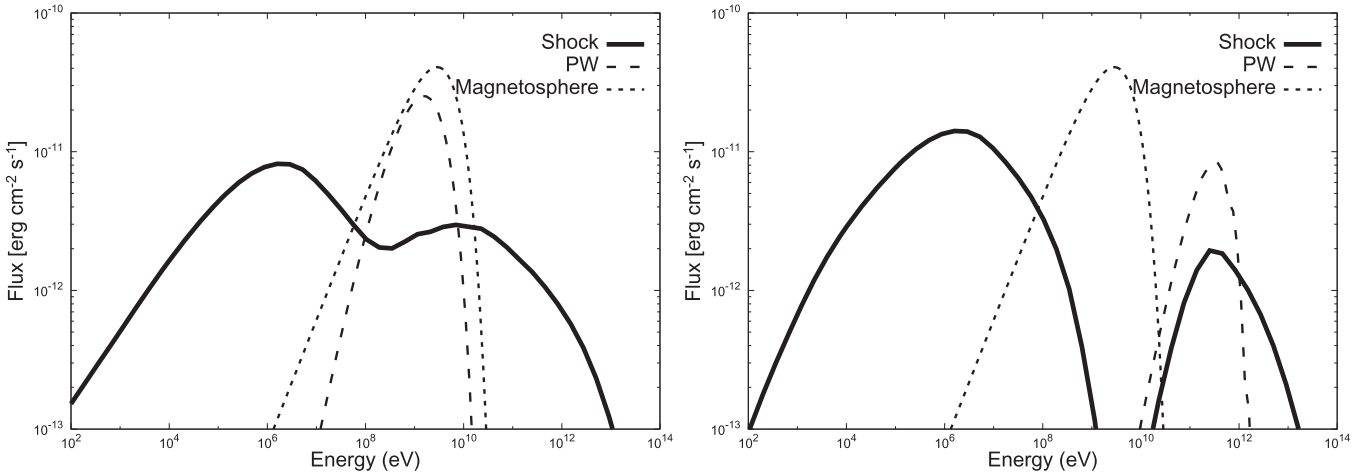

Figure 19. Multi-wavelength spectra averaged over −100 days and +100 days from the periastron and calculated with $\Gamma_{\rm PW,0} = 10^4$ in the left panel and $\Gamma_{\rm PW,0} = 10^6$ in the right panel. The calculations assume the momentum ratio $\eta = 0.02$, the power-law index $\alpha = 2$ in Equation (25), the post-shock velocity $v_{\rm pw} = v_{pw,2}$, and the Earth viewing angle $\theta_E = 60°$. The solid, dashed, and dotted line correspond to the emissions from the shocked pulsar wind, from the cold-relativistic pulsar wind, and the pulsed emissions, respectively. For the spectrum of the pulsed emissions, we apply the observational result in the *Fermi*-LAT pulsar catalog (2013).

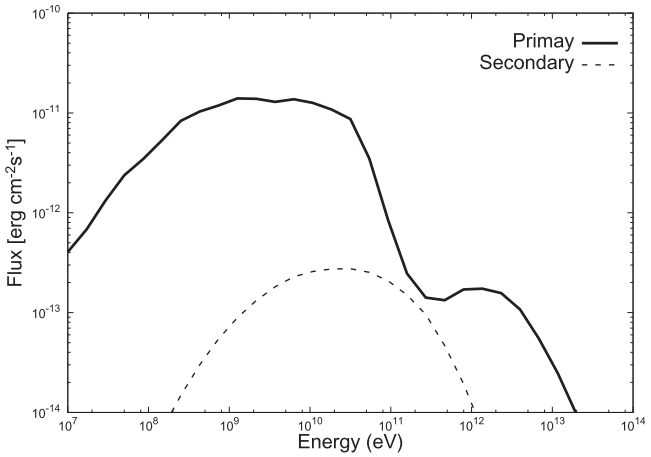

Figure 20. Comparison between the spectra of the primary (solid line) and secondary (dashed) ICS process observed on the Earth. The results are for $\sigma_0 = 0.1$, $\Gamma_{\rm PW,0} = 10^4$ and at periastron.

does not evolve with radial distance. Within the framework of the current calculation, the shock distance from the pulsar is closer, and the magnetic field at the shock is stronger for the pulsar/Be disk interaction, in which $r_s/a \sim 0.025$ at periastron, than the pulsar/Be wind interaction, for which $r_s/a \geqslant \eta^{1/2}/(1+\eta^{1/2}) \sim 0.22$ with $\eta = 0.085$. As a result, the synchrotron power is stronger for the pulsar/Be disk interaction than the pulsar/Be wind interaction. This result suggests that if the base density of the Be disk is $\rho_0 \sim 10^{-9}\,{\rm g\,cm^{-3}}$, the pulsar/Be disk interaction may give rise to a local maximum in the orbital modulation of the X-ray emissions.

As the right panel in Figure 21 shows, the calculated TeV flux for the pulsar/Be disk interaction is lower than that for the wind interaction around periastron. This is because the synchrotron cooling timescale for TeV leptons becomes shorter than the ICS cooling and adiabatic cooling timescales at the shock for the pulsar/Be disk interaction. At periastron, for example, the shock distance at the apex for the pulsar/Be wind interaction is $r_s \sim 0.22a$, for which the inverse-Compton cooling and adiabatic cooling timescales of TeV electrons are shorter than the synchrotron cooling timescale (Figure 7). For the pulsar/Be disk interaction, the shock distance becomes $r_s \sim 0.0025a$, which increases the magnetic field at the shock by a factor of ∼10, and hence decreases the synchrotron cooling timescale by about ∼1/100. As a result, the ICS cooling scale, which is less sensitive to the shock distance, becomes longer than the synchrotron timescale, and the ICS emissivity is suppressed.

5.3. Formation of a Disk Around the Pulsar

As we discussed in Section 3.2, if the base density of the disk is high enough, the pulsar wind will be confined within a small region by the Be disk matter. When the radius of the cavity estimated in Figure 6 is less than the radius below which the kinetic energy of the disk gas is less than the gravitational potential energy of the pulsar, the disk matter may be gravitationally captured by the pulsar, and results in the formation of a disk around the pulsar. The capture radius measured from the pulsar may be estimated as

$$r_{\rm cap} \sim \frac{2\,GM_N}{v_r^2} = 0.25\ {\rm au}\left(\frac{M_N}{1.4M_\odot}\right)\left(\frac{v_r}{10^7\ {\rm cm\ s^{-1}}}\right)^{-2}, \quad (27)$$

where M_N is the mass of the pulsar and v_r is the relative velocity of the pulsar with respect to the disk matter. Near periastron, the orbital velocity of the pulsar is $v_p \sim 10^7\ {\rm cm\ s^{-1}}$. The velocities of the Kepler motion and the radial velocity of the Be disk at the pulsar position are of the order of $v_{d,K}(1\ {\rm au}) \sim v_{d,K}(R_*)(R_*/1\ {\rm au})^{1/2} \sim 10^7\ {\rm cm\ s^{-1}}$ and $v_{d,r} \sim 0.1c_s \sim 10^5\ {\rm cm\ s^{-1}}$, respectively (Okazaki et al. 2011). Hence, we expect that the relative velocity is of order of $v_r \sim 10^7\ {\rm cm\ s^{-1}}$, although this depends on the disk geometry and the rotation direction.

As Figure 6 shows, near periastron, where the separation is $a \sim 1$ au, the estimated shock distance due to the pulsar/Be disk interaction is of order of $r_s \sim 0.1$ au for $\rho_0 \sim 10^{-9}\,{\rm g\,cm^{-3}}$, suggesting the disk matter could be captured by the pulsar because $r_s < r_{\rm cap}$. The accretion rate

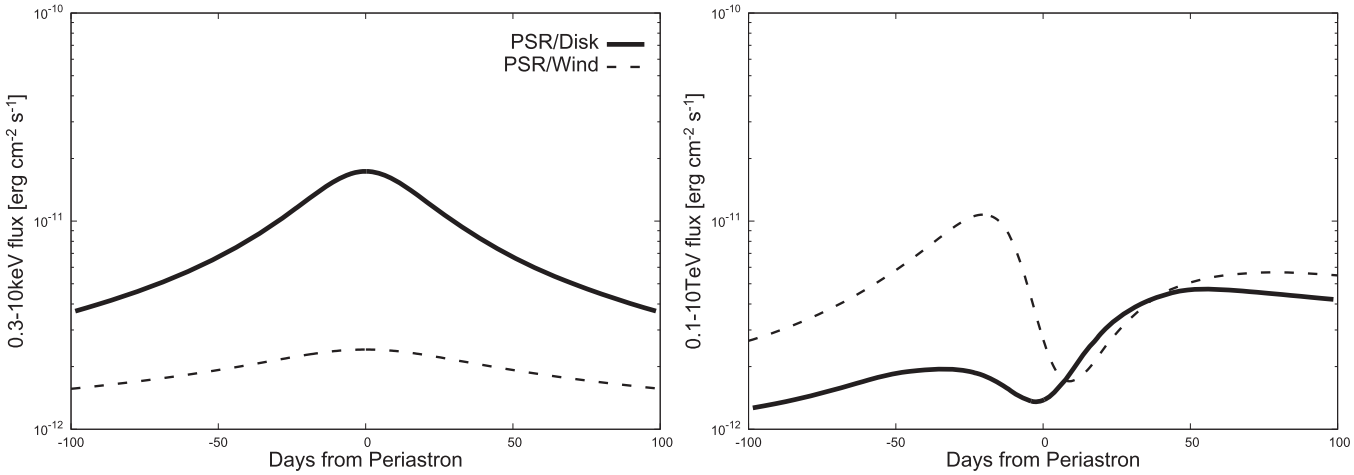

Figure 21. The solid lines show emissions from the pulsar wind stopped by the Be disk at the periastron passage. The calculations assume that all pulsar wind (4π in the solid angle) is stopped at the radial distance from the pulsar, which is given by Equation (10). For comparison, the dashed lines show the calculated light curves of the emissions from the shock due to the pulsar wind/stellar wind interaction with $\eta = 0.085$.

may be estimated as

$$\dot{M}_{\rm acc} \sim f\rho(a) r_{\rm cap}^2 v_r \sim 4 \times 10^{17}\ {\rm g\ s^{-1}} \times f\left(\frac{\rho(a)}{3\cdot 10^{-15}\ {\rm g\ cm^{-3}}}\right)\left(\frac{r_{\rm cap}}{0.25\ {\rm au}}\right)^2\left(\frac{v_r}{10^7\ {\rm cm\ s^{-1}}}\right) \quad (28)$$

where $f \sim 1$ is the geometrical factor and we used the parameter at $a \sim 1.5$ au (typical separation during the periastron passage) with $\rho_0 = 5 \times 10^{-10}\ {\rm g\ cm^{-3}}$. We note that for the stellar wind, $v_r \sim 10^8\ {\rm cm\ s^{-1}}$, the capture radius becomes $r_{\rm cap} \sim 0.0025$ au, which is usually smaller than the shock radius due to the pulsar wind and stellar wind interaction (Figure 5). Hence the stellar wind will not be captured by the pulsar.

There will be a relative angular momentum of the captured matter with respect to the pulsar, indicating the captured matter forms a circular orbit around the pulsar at a distance ($\equiv r_{\rm circ}$) where the relative angular momentum per unit mass is equal to the angular momentum of the *Kepler* orbit around the pulsar, $(GM_N r_{\rm circ})^{1/2}$. The angular frequency of the orbital motion of the pulsar is $\omega_N \sim v_p/a \sim 5 \times 10^{-7}\ {\rm rad\ s^{-1}}$. The angular frequency of the circular orbit of the Be disk around the B star is also $\omega_d \sim \omega_N$, because $v_{d,K} \sim v_p$. Roughly speaking, therefore, the angular frequency associated with the relative angular momentum will be of the order of $\omega \sim 5 \times 10^{-7}\ {\rm rad\ s^{-1}}$, although again it depends on the disk geometry and rotation direction. The circularization radius of the captured matter may be estimated as (Frank et al. 2002)

$$r_{\rm circ} \sim \frac{r_{\rm cap}^4\omega^2}{16GM_N} \sim 1.7 \times 10^{10}\ {\rm cm} \times \left(\frac{M_N}{1.4M_\odot}\right)^3\left(\frac{\omega}{5\cdot 10^{-7}\ {\rm rad\ s^{-1}}}\right)^2\left(\frac{v_r}{10^7\ {\rm cm\ s^{-1}}}\right)^{-8}. \quad (29)$$

If we apply the standard Shakura–Sunyaev disk model, the disk matter will move inward with a dynamical timescale $\tau_d(r) \sim r/v_{d,r} \sim 15$ days $\alpha_{0.1}^{-4/5}\dot{M}_{17}^{-3/10} r_{10}^{3/4}$, where $\alpha_{0.1}$ is the viscosity parameter in units of 0.1, suggesting the accreting matter will take several weeks to reach the pulsar after the capture event. If the dynamical timescale (τ_d) is longer than the pulsar's disk crossing timescale, which may be of the order of $\tau_c \sim 2H/v_p \sim 4$ days$(H/0.1\ {\rm au})(v_p/10^7\ {\rm cm\ s^{-1}})$, the accretion disk may not develop around the pulsar. We note however that the circularization radius given by Equation (29) is sensitive to the relative velocity; with $v_r \sim 2 \times 10^7$ cm, for example, $r_{\rm circ} \sim 6 \times 10^7$ cm, which is inside the light cylinder. Moreover, we do not know the geometry of the disk. If the disk plane is parallel to the orbital plane, the pulsar/Be disk continues to interact during the periastron passage. Hence it is possible that the accretion disk develops with a radial length $\sim 10^{10}$ cm around the pulsar at the periastron passage.

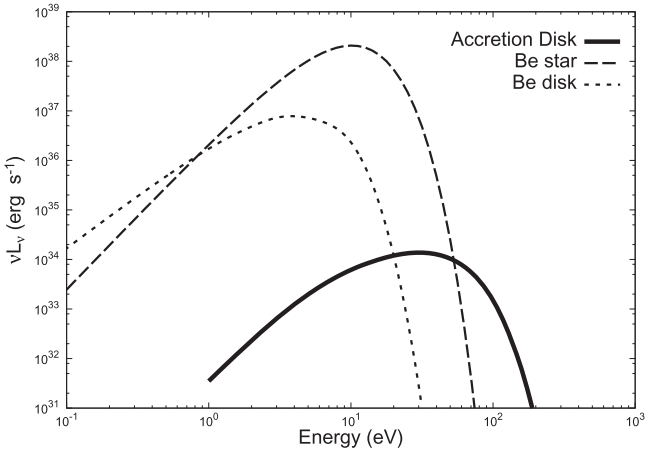

Figure 22. IR/optical/UV emissions from the PSR J2032+4127/MT91 213 system. Solid line: emissions from the Shakura–Sunyaev disk with $\dot{M} = 4 \times 10^{17}\ {\rm g\ s^{-1}}$ and the disk extends from $r = 7 \times 10^8$ cm to 10^{10} cm. Dashed line: blackbody emission from the stellar surface with temperature $T_* = 30{,}000$ K. We assume the Planck function. Dotted line: blackbody radiation from the isothermal Be disk with the temperature $T_d = 0.6T_*$ (Carciofi & Bjorkman 2006).

If the accretion disk forms around the pulsar, the disk supplies UV photons in the pulsar wind region. Figure 22 summarizes the radiation power (νL_ν) for the accretion disk (solid line), stellar surface (dashed line), and Be disk (dotted line). For the accretion disk, we assume an accretion rate $\dot{M} = 4 \times 10^{17}\ {\rm g\ s^{-1}}$ and the disk extends from the light cylinder $r = r_{\rm lc}$ of the pulsar to $r = 10^{10}$ cm. For the stellar

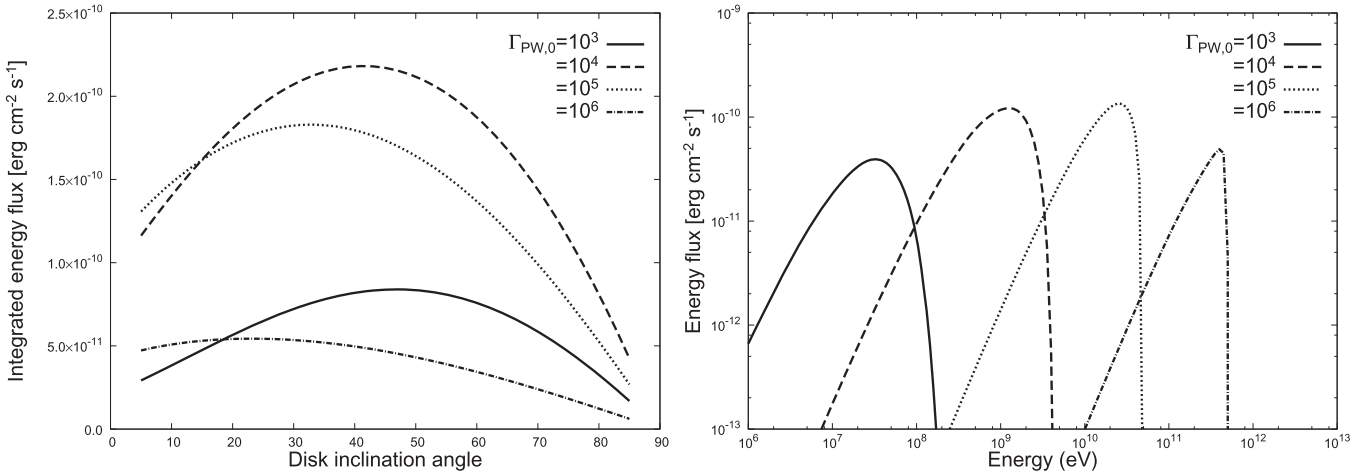

Figure 23. The calculated ICS process between the cold-relativistic pulsar wind and the soft photons from the accretion disk around the pulsar. Left: the integrated flux for the different Lorentz factor of the pulsar wind as a function of the disk inclination angle, which is the angle between the Earth direction and direction perpendicular to the disk plane. In the calculation, the disk extends from $r = r_{\rm LC}$ to $r = 10^{10}$ cm. Right: the calculated spectra for the disk inclination angle $\theta_i = 45°$.

emission, we assume the Planck function with T_*= 30,000 K and $R_* = 10R_\odot$. For the Be disk emissions, we assumed a disk temperature $T_d = 0.6T_*$ after the calculation of Carciofi & Bjorkman (2006). We ignore the effects of the emission and absorption lines on the spectra.

As discussed in above, the captured matter will take about several weeks to reach the pulsar magnetosphere. Before the accretion disk reaches the light cylinder radius, the rotation of the pulsar is still active and produces the cold-relativistic pulsar wind. Then we can expect that the ICS process of the cold-relativistic pulsar will boost up the UV photons from the disk to higher energy. Figure 23 summarizes the calculated spectra (left panel) and the integrated flux as a function of the accretion disk inclination angle (right panel). The figure shows the results when the accretion disk extends from the light cylinder radius $r = r_{\rm lc}$ to $r = 10^{10}$ cm. In addition, we assumed a mono-energetic distribution of the particles in the cold-relativistic pulsar wind, and took into account the energy loss of the pulsar wind due to the ICS process. As Figure 23 shows, if the initial Lorentz factor is $\Gamma_0 = 10^{4-5}$ which produces the scattered photons with 1–10 GeV energy, the calculated flux level can reach an order of 2×10^{-10} erg cm^{-2} s^{-1}, which is comparable to that of the pulsed emissions.

Pulsar binary systems may provide a valuable laboratory to study the accretion process on rapidly spinning and strongly magnetized neutron stars. One may consider that once the accretion disk crosses the light cylinder, the rotation-powered activity would be quenched. This is because copious plasma fills the acceleration region at the rotation-powered stage, where the charge density deviates from the so-called Goldreich–Julian charge density (Goldreich & Julian 1969). However, recent observation suggests the rotation-powered activity and the accretion disk can co-exist in the magnetosphere. A transient-millisecond pulsar is a binary millisecond pulsar with a low-mass companion star, and it transits between the rotation-powered stage and the accretion stage (Archibald et al. 2009). PSR J1023+0038 transited from the former stage to the latter in 2013 June, when the pulsed radio emission from this pulsar disappeared (Stappers et al. 2011). Coherent pulsed X-ray emission discovered after 2013 June suggests an accretion of matter on the neutron star surface (Archibald et al. 2015). Jaodand et al. (2016), however, found that the spin-down rate in the accretion stage is higher than that in the rotation-powered stage, and they concluded that the rotation activity is still operating in the accretion stage. Enhancement of observed GeV emission in the accretion stage also suggests the survival of rotation activity in the accretion stage (Takata et al. 2014b). This model was also applied to another transient-millisecond pulsar PSR J1227–4853 (Bednarek 2015). Gamma-ray binaries with a Be companion may also offer opportunities to study this accretion process on young pulsars.

The ICS model of the pulsar wind could provide an explanation for the origin of the flare-like GeV emissions from PSR B1259–63/LS 2883 system after the second Be disk passage of the pulsar. It has been observed that the GeV peak in the orbital modulation occurs ∼20 days after the X-ray peak (Tam et al. 2011, 2015). It has been considered that the phase of the X-ray peak corresponds to that of the pulsar/Be disk interaction. So we may expect that the Be disk matter starts to be captured by the pulsar at around the orbital phase of the X-ray peak. Since it will take several weeks to fully develop the accretion disc around the pulsar, the GeV peak position will delay the X-ray peak position.

Finally, the magnetic radius r_M from the pulsar is defined as the distance where the dipole magnetic field of the pulsar begins to dominate the dynamics of the accreting matter, and it is estimated from $B^2(r_M)/8\pi = \rho_{\rm acc} v^2$ with $\rho_{\rm acc} v = \dot{M}/4\pi r_M^2$ and $v \sim (2GM_N/r_M)^{1/2}$,

$$r_M \sim 3 \times 10^8 \,{\rm cm} \left(\frac{B_s}{10^{12}{\rm G}}\right)^{4/7} \times \left(\frac{\dot{M}}{10^{17}\,{\rm g\,cm^{-3}}}\right)^{-2/7} \left(\frac{M_N}{1.4M_\odot}\right)^{-1/7}. \quad (30)$$

This radius is smaller than the light cylinder radius of PSR J2032+4127 ($r_{\rm lc} = 6.8 \times 10^8$ cm). The co-rotation radius ($r_{\rm co}$) is defined as the distance where the angular velocity of Keplerian motion is equal to the spin angular

velocity of the pulsar, namely

$$r_{\rm co} = \left(\frac{GMP^2}{4\pi^2}\right)^{1/3} \sim 4.6 \times 10^7 \ {\rm cm} \left(\frac{P}{0.143 \ {\rm ms}}\right)^{2/3} \left(\frac{M_N}{1.4 M_\odot}\right)^{1/3}, \quad (31)$$

which will be smaller than the magnetic radius, suggesting the accretion process is in a propeller regime, and not all infalling matter will accrete on the pulsar surface. The outflow due to the propeller effect also could cause the high-energy emission (e.g., Papitto & Torres 2015).

In summary, we analyzed *Swift* and *Fermi*-LAT data of thePSR J2032+4127/MT91 213 binary system, which is a candidate to be another TeV gamma-ray binary. The X-ray flux has rapidly increased as the pulsar approaches periastron, which will occur in late 2017 or early 2018, while the GeV flux measured by *Fermi*-LAT shows no significant change. We investigated the X-ray emission by the synchrotron process of the pulsar wind particles accelerated at the shock due to the pulsar wind and stellar wind interaction. We argued that the increase in the observed X-rays is caused by (1) variation of the momentum ratio of the two winds along the orbital phase or (2) the evolution of the magnetization parameter of the pulsar wind with radial distance as $\sigma(r) \propto r^{-\alpha}$ and $\alpha \sim 2$–3. The current model predicts that the peak fluxes in the 0.3–10 keV and 0.1–10 TeV energy bands are of the order of $\sim 10^{-11}$ erg cm^{-2} s^{-1}. The gamma-ray binary system could provide a unique laboratory to study the emissions from the cold-relativistic pulsar wind. The current model suggests that the ICS process of the cold-relativistic pulsar wind could contribute to the *Fermi*-LAT observations at the periastron passage (Figure 18). For this binary system, the pulsar/Be disk interaction will affect the observed emissions, provided that the base density of the Be disk is $\rho_0 > 10^{-10}$ g cm^{-3} and the interaction occurs during ~ -100 days and $\sim +100$ days. For a Be disk with higher base density $\rho_0 \sim 10^{-9}$ g cm^{-3}, the pulsar/Be disk interaction could form an accretion disk around the pulsar. The ICS process of the cold-relativistic pulsar wind of the UV from the disk also provides high-energy emission from the pulsar/Be star binary system. Future multi-wavelength observations will provide a unique opportunity to probe the pulsar wind properties and the various emission processes caused by the pulsar/Be wind and pulsar/Be disk interactions.

We express our appreciation to an anonymous referee for useful comments and suggestions. We thank A. Okazaki for the useful discussions on the Be disk model. J.T. is supported by NSFC grants of Chinese Government under 11573010 and U1631103. C.W.N. and K.S.C. are supported by GRF grant under 17302315. C.Y.H. is supported by the National Research Foundation of Korea through grants 2014R1A1A2058590 and 2016R1A5A1013277. All calculations were done under the High Performance Computing Cluster (Hyperion) of the Institute of Particle Physics and Astrophysics, HUST.

References

Abdo, A. A., Ackermann, M., Ajello, M., et al. 2009, ApJL, 706, 56
Abdo, A. A., Ackermann, M., Ajello, M., et al. 2011, ApJL, 736, 11
Abdo, A. A., Ajello, M., Allafort, A., et al. 2013, ApJS, 208, 17
Acero, F., Ackermann, M., Ajello, M., et al. 2015, ApJS, 218, 23
Ackermann, M., Ajello, M., Ballet, J., et al. 2012, Sci, 335, 189
Aharonian, F., Akhperjanian, A. G., Aye, K.-M., et al. 2005, A&A, 442, 1
Aharonian, F., Akhperjanian, A. G., Bazer-Bachi, A. R., et al. 2006, A&A, 460, 743
Albert, J., Aliu, E., Anderhub, H., et al. 2006, Sci, 312, 1771
Archibald, A. M., Bogdanov, S., Patruno, A., et al. 2015, ApJ, 807, 62
Archibald, A. M., Stairs, I. H., Ransom, S. M., et al. 2009, Sci, 324, 1411
Bednarek, W. 1997, A&A, 322, 523
Bednarek, W. 2000, A&A, 362, 646
Bednarek, W. 2007, A&A, 464, 259
Bednarek, W. 2015, MNRAS, 451, 55
Bogovalov, S. V., & Khangoulian, D. V. 2002, MNRAS, 336, 53
Bogovalov, S. V., Khangulyan, D. V., Koldoba, A. V., Ustyugova, G. V., & Aharonian, F. A. 2008, MNRAS, 387, 63
Bosch-Ramon, V. 2013, A&A, 560, 32
Bozzo, E., Oskinova, L., Feldmeier, A., & Falanga, M. 2016, A&A, 589, 102
Camilo, F., Ray, P. S., Ransom, S. M., et al. 2009, ApJ, 705, 1
Canto, J., Raga, A. C., & Wilkin, F. P. 1996, ApJ, 469, 729
Carciofi, A. C., & Bjorkman, J. E. 2006, ApJ, 639, 1081
Casandjian, J.-M., & Grenier, I. A. 2008, A&A, 489, 849
Cerutti, B., Dubus, G., & Henri, G. 2008, A&A, 488, 37
Cerutti, B., Malzac, J., Dubus, G., & Henri, G., 2010, A&A, 519, 81
Chernyakova, M., Neronov, A., Lutovinov, A., Rodriguez, J., & Johnston, S. 2006, MNRAS, 367, 1201
Chernyakova, M., Neronov, A., van Soelen, B., et al. 2015, MNRAS, 454, 1358
de la Cita, V. M., Bosch-Ramon, V., Paredes-Fortuny, X., Khangulyan, D., & Perucho, M. 2017, A&A, 598, A13
Dickey, J. M., & Lockman, F. J. 1990, ARA&A, 28, 215
Dubus, G. 2006, A&A, 456, 801
Dubus, G. 2013, A&ARv, 21, 64
Dubus, G., & Cerutti, B. 2013, A&A, 557, 127
Dubus, G., Cerutti, B., & Henri, G. 2008, A&A, 477, 691
Dubus, G., Cerutti, B., & Henri, G. 2010, A&A, 516, 18
Evans, P. A., Beardmore, A. P., Page, K. L., et al. 2007, A&A, 469, 379
Evans, P. A., Beardmore, A. P., Page, K. L., et al. 2009, MNRAS, 3, 1177
Frank, J., King, A., & Raine, D. 2002, Accretion Power in Astrophysics (Cambridge: Cambridge Univ. Press)
Georgy, C., Meynet, G., & Maeder, A. 2011, A&A, 527, 52
Goldreich, P., & Julian, W. H. 1969, ApJ, 157, 869
Hibschman, J. A., & Arons, J. 2001, ApJ, 554, 624
Hinton, S., Skilton, J. L, Funk, S., et al. 2009, ApJL, 690L, 101
Ho, W. C. G., Ng, C.-Y., Lyne, A. G., et al. 2017, MNRAS, 464, 1211
Jaodand, A., Archibald, A. M., Hessels, J. W. T., et al. 2016, ApJ, 830, 122
Johnston, S., Ball, L., Wang, N., & Manchester, R. N. 2005, MNRAS, 358, 1069
Johnston, S., Manchester, R. N., McConnell, D., & Campbell-Wilson, D. 1999, MNRAS, 302, 277
Johnston, Simon, Manchester, R. N., Lyne, A. G., et al. 1992, ApJL, 387, 37
Kalberla, P. M. W., Burton, W. B., Hartmann, D., et al. 2005, A&A, 440, 775
Kapala, M., Bulik, T., Rudak, B., Dubus, G., & Lyczek, M. 2010, in Proc. XXV Texas Symp. on Relativistic Astrophysics, ed. F. M. Rieger (Chair), C. van Eldik, & W. Hofmann (Trieste: SISSA) http://pos.sissa.it/cgi-bin/reader/conf.cgi?confid=123, id.193
Kennel, C. F., & Coroniti, F. V. 1984, ApJ, 283, 710
Khangulyan, D., Aharonian, F. A., Bogovalov, S. V., & Ribó, M. 2011, ApJ, 742, 98
Khangulyan, D., Aharonian, F. A., Bogovalov, S. V., & Ribó, M. 2012, ApJL, 752, 17
Khangulyan, D., Bogovalov, S. V., & Aharonian, F. A. 2014, IJMPS, 28, 60169
Khangulyan, D., Hnatic, S., Aharonian, F. A., & Bogovalov, S. V. 2007, MNRAS, 380, 320
Kirk, J. G., Ball, L., & Skjæraasen, O. 1999, APh, 10, 31
Kong, S. W., Cheng, K. S., & Huang, Y. F. 2012, ApJ, 753, 127
Kong, S. W., Yu, Y. W., Huang, Y. F., & Cheng, K. S. 2011, MNRAS, 416, 1067
Lee, Umin, Osaki, Yoji, & Saio, Hideyuki 1991, MNRAS, 250, 432
Lyne, A. G., Stappers, B. W., Keith, M. J., et al. 2015, MNRAS, 451, 581
Negueruela, I., Ribó, M., Herrero, A., et al. 2011, ApJL, 732, L11
Okazaki, A. T., Nagataki, S., Naito, T., et al. 2011, PASJ, 63, 893
Owocki, S. P., & Cohen, D. H. 2006, ApJ, 648, 565
Owocki, S. P., Romero, G. E., Townsend, R. H. D., & Araudo, A. T. 2009, ApJ, 696, 690
Papitto, A., & Torres, D. F. 2015, ApJ, 807, 33
Runacres, M. C., & Owocki, S. P. 2002, A&A, 381, 1015
Sefako, R. R., & de Jager, O. C. 2003, ApJ, 593, 1013

Sierpowska, A., & Bednarek, W. 2005, MNRAS, 356, 711
Sierpowska-Bartosik, A., & Bednarek, W. 2008, MNRAS, 385, 2279
Sierpowska-Bartosik, A., & Torres, D. F. 2007, ApJL, 671, L145
Sierpowska-Bartosik, A., & Torres, D. F. 2008, APh, 30, 239
Smith, M. A. 2006, A&A, 459, 215
Snow, T. P., Jr. 1981, ApJ, 251, 139
Stappers, B. W., Archibald, A., Bassa, C., et al. 2011, ATel, 5513, 1
Takahashi, T., Kishishita, T., Uchiyama, Y., et al. 2009, ApJ, 697, 592
Takata, J., Leung, G. C. K., Tam, P. H. T., et al. 2014a, ApJ, 790, 18
Takata, J., Li, K. L., Leung, G. C. K., et al. 2014b, ApJ, 785, 131
Takata, J., Okazaki, A. T., Nagataki, S., et al. 2012, ApJ, 750, 70
Takata, J., & Taam, R. E. 2009, ApJ, 702, 100
Tam, P. H. T., Huang, R. H. H., Takata, J., et al. 2011, ApJL, 736, 10
Tam, P. H. T., Li, K. L., Takata, J., et al. 2015, ApJ Letter, 798, 26
Tanaka, S. J., & Takahara, F. 2010, ApJ, 715, 1248
Tavani, M., & Arons, J. 1997, ApJ, 477, 439
Timokhin, A. N., & Harding, A. K. 2015, ApJ, 810, 144
Torres, D. F. 2011, arXiv:1008.0483
van Soelen, B., Meintjes, P. J., Odendaal, A., & Townsend, L. J. 2012, MNRAS, 426, 3135
Walder, R., Folini, D., & Meynet, G. 2012, SSRv, 166, 145
Waters, L. B. F. M., van den Heuvel, E. P. J., Taylor, A. R., Habets, G. M. H. J., & Persi, P. 1988, A&A, 198, 200
Xing, Y., Wang, Z., & Takata, J. 2016, ApJ, 828, 61
Yamaguchi, M. S., & Takahara, F. 2010, ApJ, 717, 85
Yamaguchi, M. S., & Takahara, F. 2012, ApJ, 761, 146
Zabalza, V., Bosch-Ramon, V., Aharonian, F., & Khangulyan, D. 2013, A&A, 551, 17